Generalized Huygens principle with pulsed-beam wavelets

2009 J. Phys. A: Math. Theor. 42 475403

(http://iopscience.iop.org/1751-8121/42/47/475403)

IOP PUBLISHING JOURNAL OF PHYSICS A: MATHEMATICAL AND THEORETICAL

J. Phys. A: Math. Theor. **42** (2009) 475403 (33pp) doi:10.1088/1751-8113/42/47/475403

Generalized Huygens principle with pulsed-beam wavelets

Thorkild Hansen[1] **and Gerald Kaiser**[2]

[1] Seknion Inc., Boston, MA, USA
[2] Signals & Waves, Austin, TX, USA

E-mail: thorkild.hansen@att.net and kaiser@wavelets.com

Received 23 July 2009
Published 6 November 2009
Online at stacks.iop.org/JPhysA/42/475403

Abstract

Huygens' geometric construction explaining wave motion has a well-known problem with unphysical back-propagation due to the spherical nature of the secondary wavelets. We solve this by analytically continuing the surface of integration. If the surface is a sphere S_R of radius R, this is done by complexifying R to $\alpha = R + \mathrm{i}a$. The resulting complex sphere S_α is shown to be equivalent to the real tangent disk bundle with base S_R consisting of all disks with radius a tangent to S_R. Huygens' secondary source points are thus replaced by disks, and his secondary wavelets by well-focused pulsed beams propagating outward. This solves the back-propagation problem. The generalized Huygens principle is a *completeness relation* for these pulsed-beam wavelets enabling a *pulsed-beam representation* of all radiation fields. Furthermore, this yields a natural and extremely efficient way to compute radiation fields *numerically* because all pulsed beams missing a given observer can be ignored with minimal error. Increasing the disk radius a sharpens the focus of the pulsed beams, which in turn raises the *compression ratio* of the representation.

PACS numbers: 03.50.De, 41.20.Jb, 42.25.Bs

(Some figures in this article are in colour only in the electronic version)

1. Introduction

Huygens' principle[3] [BC87] states that the solution of the wave equation radiated by a bounded source can be represented outside the source region as a superposition of spherical *Huygens wavelets* radiated by secondary point-sources on a surface enclosing the primary source. This was originally proposed as an intuitive explanation of wave propagation, but as such it is

[3] Also known as the *Huygens–Fresnel* principle following the important analytical contributions by Augustin Jean Fresnel complementing Huygens' geometric construction.

conceptually problematic because the spherical wavelets propagate equally in all directions, thus implying that the wave propagates *backward* (toward the source) as well as forward (away from the source). We propose a solution to this problem by generalizing the idea of Huygens wavelets.

Choosing the surface to be the sphere S_R of radius R, we show that the Huygens representation of the exterior wave can be continued analytically to a complex radius $\alpha = R+ia$. For any unit vector $\hat{\boldsymbol{n}}$, the complex vector $\alpha\hat{\boldsymbol{n}}$ is shown to represent a *real* disk of radius a tangent to S_R at the point $R\hat{\boldsymbol{n}}$. The complex sphere $S_\alpha \subset \mathbb{C}^3$ consisting of all such vectors $\alpha\hat{\boldsymbol{n}}$ is thus equivalent to a real *tangent disk bundle* with base S_R. Just as the points $R\hat{\boldsymbol{n}} \in S_R$ radiate spherical wavelets, so do the tangent disks $\alpha\hat{\boldsymbol{n}} \in S_\alpha$ radiate well-focused *pulsed-beam wavelets* propagating in the outward direction $\hat{\boldsymbol{n}}$. The analytically continued Huygens formula can be given the following real interpretation: the interior wave radiated by the source is *intercepted* by the set of tangent disks, which then re-radiate it as a set of outgoing pulsed beams. The original wave is thus represented in the exterior as a superposition of pulsed beams emanating from disks tangent to S_R, and the coefficients in this superposition are interpreted as local *reception amplitudes* by the disks.

The generalized Huygens principle is a *completeness relation* for pulsed-beam wavelets enabling a *pulsed-beam representation* of radiation fields. Since the new wavelets can be *focused* by increasing the disk radius a, our construction solves the directionality problem of Huygens' construction. Furthermore, it leads naturally to substantial gains in the efficiency of computing radiation fields numerically. Only pulsed beams propagating toward the observer need to be included in the expansion, and the rest can be ignored while incurring minimal errors. This leads to a significantly *compressed* representation of radiation fields, with the amount of compression controlled by the disk radius a.

The plan of the paper is as follows. In section 2, we review Huygens' principle for time-harmonic waves. In section 3, we introduce the idea of *complex distance* and show that the complex sphere S_{R+ia} is equivalent to a bundle of disks of radius a tangent to the real sphere S_R. In section 4, we continue Huygens' principle for time-harmonic waves analytically from S_R to S_α and show that each disk $\alpha\hat{\boldsymbol{n}} \in S_\alpha$ radiates a beam propagating outward along the direction of $\hat{\boldsymbol{n}}$. In section 5, we introduce the *Gaussian pulsed-beam propagator*, an analytic extension of the usual propagator representing wave propagation from a disk to a point, and use it to prove the generalized Huygens principle in the time domain. In section 6, we investigate the associated pulsed-beam Huygens wavelets. Section 7 consists of some additional remarks on the pulsed-beam nature of these wavelets. In section 8, we establish the *Huygens reproducing relation* for pulsed-beam wavelets, showing that wave propagation from an emission event x_e inside S_R to a reception event x_r outside S_R can be expressed as an integral of products of pulsed-beam propagators from x_e to z and z to x_r, where z is an intermediate event representing interception and re-emission by a disk $\alpha\hat{\boldsymbol{n}} \in S_\alpha$. In section 9, we present the generalized Huygens principle for arbitrary sources. In section 10, we prove that the coefficients in the pulsed-beam representation of a radiation field are the reception amplitudes of the interior wave by the disks $\alpha\hat{\boldsymbol{n}} \in S_\alpha$, thus completing the physical interpretation of the generalized Huygens principle. In section 11, we demonstrate the numerical advantages of the pulsed-beam representation by confirming that its numerical compression increases with the disk radius a.

Note that the term 'wavelets' is used here in its original meaning related to Huygens' principle and has no direct connection to the modern concepts of wavelets [K94]. However, it can be shown that our generalized Huygens wavelets give a *time-frequency analysis* specifically adapted to solutions of the wave equation. This connection will be explained elsewhere.

2. Huygens principle for time-harmonic waves

Consider a time-harmonic source ϱ of frequency ω supported in a bounded volume $V \subset \mathbb{R}^3$:

$$\varrho(\boldsymbol{x}, t) = \mathrm{Re}\{\mathrm{e}^{-\mathrm{i}\omega t}\varrho_\omega(\boldsymbol{x})\}, \qquad \mathrm{supp}\,\varrho_\omega \subset V.$$

The wave radiated in free space and observed at the *reception event* $(\boldsymbol{x}_r, t_r)$ is

$$F(\boldsymbol{x}_r, t_r) = \mathrm{Re}\{\mathrm{e}^{-\mathrm{i}\omega t_r} F_\omega(\boldsymbol{x}_r)\} \qquad \text{with} \qquad F_\omega(\boldsymbol{x}_r) = \int \mathrm{d}\boldsymbol{x} G_\omega(\boldsymbol{x}_r - \boldsymbol{x})\varrho_\omega(\boldsymbol{x}),$$

where

$$G_\omega(\boldsymbol{r}) = \frac{\mathrm{e}^{\mathrm{i}\omega r}}{r}, \qquad r = |\boldsymbol{r}| \tag{1}$$

is the outgoing fundamental solution of the Helmholtz equation:

$$(\nabla^2 + \omega^2)G_\omega(\boldsymbol{x}) = -4\pi\delta(\boldsymbol{x}). \tag{2}$$

We are using units in which the constant wave propagation speed $c = 1$, so the wave number is $k \equiv \omega/c = \omega$.

Let S be a smooth surface containing V in its interior. Green's second identity, combined with (2), shows that F_ω is given in the *exterior* of S by

$$F_\omega(\boldsymbol{x}_r) = -\frac{1}{4\pi}\int_S \mathrm{d}S(\boldsymbol{x}) G_\omega(\boldsymbol{x}_r - \boldsymbol{x})\overleftrightarrow{\partial}_n F_\omega(\boldsymbol{x}), \tag{3}$$

where $\mathrm{d}S$ is the area measure on S and we have introduced the notation

$$g(\boldsymbol{x})\overleftrightarrow{\partial}_n f(\boldsymbol{x}) = g(\boldsymbol{x})\partial_n f(\boldsymbol{x}) - \partial_n g(\boldsymbol{x}) f(\boldsymbol{x}),$$

where ∂_n is the outward normal derivative at $\boldsymbol{x} \in S$. Equation (3) is a precise expression of *Huygens' principle* as formulated by Kirchhoff [BC87, BW99]. It states that in the exterior region, $F_\omega(\boldsymbol{x}_r)$ can be represented as a superposition of the spherical waves $G_\omega(\boldsymbol{x}_r - \boldsymbol{x})$, called *Huygens wavelets*, together with their normal derivatives. Hence, the points $\boldsymbol{x} \in S$ act as secondary sources which collectively form a surface source *equivalent* to the original source ϱ_ω in the exterior region[4].

Equation (3) can be expressed as a condition on the fundamental solution G_ω by letting ϱ_ω be a point source

$$\varrho_\omega(\boldsymbol{x}) = \delta(\boldsymbol{x} - \boldsymbol{x}_e),$$

with $\boldsymbol{x}_e$ in the interior of S. Then, $F_\omega(\boldsymbol{x}) = G_\omega(\boldsymbol{x} - \boldsymbol{x}_e)$; hence, (3) becomes

$$G_\omega(\boldsymbol{x}_r - \boldsymbol{x}_e) = -\frac{1}{4\pi}\int_S \mathrm{d}S(\boldsymbol{x}) G_\omega(\boldsymbol{x}_r - \boldsymbol{x})\overleftrightarrow{\partial}_n G_\omega(\boldsymbol{x} - \boldsymbol{x}_e). \tag{4}$$

We call (4) the *Huygens reproducing relation* for G_ω. To recover (3), multiply by a general source density $\varrho_\omega(\boldsymbol{x}_e)$ supported inside S and integrate over $\boldsymbol{x}_e$. We shall generalize Huygens' principle by continuing analytically in the integration variable $\boldsymbol{x}$, and for this purpose it will be more convenient to work with (4) than (3). This will be done in the special case where S is the sphere of radius R centered at the origin,

$$S_R = \{\boldsymbol{x} = R\hat{\boldsymbol{n}} : \hat{\boldsymbol{n}} \in S^2\},$$

where S^2 denotes the unit sphere. Then,

$$\mathrm{d}S(\boldsymbol{x}) = R^2\,\mathrm{d}\hat{\boldsymbol{n}}, \qquad \text{where} \quad \mathrm{d}\hat{\boldsymbol{n}} = \sin\theta\,\mathrm{d}\theta\,\mathrm{d}\phi$$

[4] The equivalent surface source consists of a *single layer* $\{G_\omega\partial_n f\}$ and a *double (dipole) layer* $\{-\partial_n G_\omega\, f\}$.

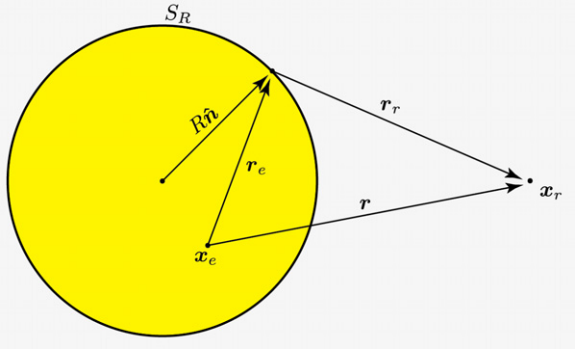

Figure 1. The sphere S_R, the emission and reception points $\boldsymbol{x}_e$, $\boldsymbol{x}_r$, and the vectors $\boldsymbol{r}_e$, $\boldsymbol{r}_r$.

is the area measure on S^2; hence, (4) becomes

$$G_\omega(\boldsymbol{r}) = -\frac{R^2}{4\pi}\int \mathrm{d}\hat{\boldsymbol{n}} G_\omega(\boldsymbol{r}_r)\overleftrightarrow{\partial}_R G_\omega(\boldsymbol{r}_e), \qquad |\boldsymbol{x}_e| < R < |\boldsymbol{x}_r|, \tag{5}$$

where

$$\boldsymbol{r}_e = R\hat{\boldsymbol{n}} - \boldsymbol{x}_e, \qquad \boldsymbol{r}_r = \boldsymbol{x}_r - R\hat{\boldsymbol{n}}, \qquad \boldsymbol{r} = \boldsymbol{r}_e + \boldsymbol{r}_r = \boldsymbol{x}_r - \boldsymbol{x}_e \tag{6}$$

as seen in figure 1. The normal derivative $\partial_n = \hat{\boldsymbol{n}}\cdot\nabla$ has been replaced by the partial derivative ∂_R, and

$$\begin{aligned} G_\omega(\boldsymbol{r}_e) &= \frac{\mathrm{e}^{\mathrm{i}\omega r_e}}{r_e}, \qquad r_e = |\boldsymbol{r}_e|, \qquad \partial_R r_e = \frac{R - \hat{\boldsymbol{n}}\cdot\boldsymbol{x}_e}{r_e} \\ G_\omega(\boldsymbol{r}_r) &= \frac{\mathrm{e}^{\mathrm{i}\omega r_r}}{r_r}, \qquad r_r = |\boldsymbol{r}_r|, \qquad \partial_R r_r = \frac{R - \hat{\boldsymbol{n}}\cdot\boldsymbol{x}_r}{r_r}. \end{aligned} \tag{7}$$

We shall complexify the points $R\hat{\boldsymbol{n}}$ of S_R by complexifying R and proving that this gives an analytic continuation of the distances r_e and r_r, hence of the right-hand side in (5). In the next section, we show that this procedure has a surprising and beautiful geometric interpretation in *real* space.

3. The complex sphere as a tangent disk bundle

Let $\alpha = R + \mathrm{i}a \in \mathbb{C}$ with $a > 0$, and consider the complexifications of (6),

$$\boldsymbol{r}_e \to \boldsymbol{z}_e = \alpha\hat{\boldsymbol{n}} - \boldsymbol{x}_e = \boldsymbol{r}_e + \mathrm{i}a\hat{\boldsymbol{n}}, \qquad \boldsymbol{r}_r \to \boldsymbol{z}_r = \boldsymbol{x}_r - \alpha\hat{\boldsymbol{n}} = \boldsymbol{r}_r - \mathrm{i}a\hat{\boldsymbol{n}}, \tag{8}$$

regarded as analytic functions of α. To continue $G_\omega(\boldsymbol{r}_e)$ and $G_\omega(\boldsymbol{r}_r)$ in (5) to $\mathbb{C}^3$, we must continue the distances r_e , r_r analytically in α. We will first explain the continuation of r_r in detail and then derive the corresponding expressions for r_e.

The *complex distance* from $\alpha\hat{\boldsymbol{n}}$ to $\boldsymbol{x}_r$ is defined by

$$\zeta_r = \sqrt{w}, \qquad \text{where} \quad w = \boldsymbol{z}_r\cdot\boldsymbol{z}_r = r_r^2 - a^2 - 2\mathrm{i}a\boldsymbol{r}_r\cdot\hat{\boldsymbol{n}}. \tag{9}$$

ζ_r will be regarded *in parallel* as an analytic function of $\boldsymbol{z}_r \in \mathbb{C}^3$ and as a complex function of $\boldsymbol{x}_r \in \mathbb{R}^3$ with $\alpha\hat{\boldsymbol{n}} \in \mathbb{C}^3$ fixed. Any analytic function $f(\boldsymbol{x}_r)$ depending only on r_r can be continued analytically to some domain in $\mathbb{C}^3$ by substituting $r_r \to \zeta_r$, and we shall regard this as a *deformation*

$$f(\boldsymbol{x}_r) \to f_{\alpha\hat{\boldsymbol{n}}}(\boldsymbol{x}_r) \equiv f(\boldsymbol{x}_r - \alpha\hat{\boldsymbol{n}}). \tag{10}$$

Since $f_{\alpha\hat{\boldsymbol{n}}}$ is analytic in α, this deformation *preserves solutions of differential equations* such as (2).[5] The deformation breaks the spherical symmetry of r_r. Coupled with a similar deformation of other variables such as r_e, this will provide a powerful mathematical tool for generating nontrivial and *interesting* solutions from simple spherical ones. Furthermore, the *singularities* of deformed solutions give rise to their deformed *sources* [K3].

Being defined in terms of the complex square root, ζ_r is double-valued. To make it single-valued, a branch cut must be introduced and a branch chosen. In the complex variable $w \in \mathbb{C}$, we choose the standard branch cut of $\sqrt{w}$ along the negative real axis $w \leqslant 0$. But

$$w \leqslant 0 \quad \Leftrightarrow \quad \{r_r \leqslant a, \hat{\boldsymbol{n}} \cdot \boldsymbol{r}_r = 0\} \quad \Leftrightarrow \quad \{|\boldsymbol{x}_r - R\hat{\boldsymbol{n}}| \leqslant a, \hat{\boldsymbol{n}} \cdot (\boldsymbol{x}_r - R\hat{\boldsymbol{n}}) = 0\};$$

hence, the branch cut of ζ_r as a function of $\boldsymbol{x}_r \in \mathbb{R}^3$ with $\alpha\hat{\boldsymbol{n}} \in \mathbb{C}^3$ fixed is

$$\begin{aligned} \mathcal{D}(\alpha\hat{\boldsymbol{n}}) &= \{\boldsymbol{x}_r : r_r \leqslant a,\ \hat{\boldsymbol{n}} \cdot \boldsymbol{r}_r = 0\} \\ &= \{\boldsymbol{x}_r : |\boldsymbol{x}_r - R\hat{\boldsymbol{n}}| \leqslant a,\ \hat{\boldsymbol{n}} \cdot (\boldsymbol{x}_r - R\hat{\boldsymbol{n}}) = 0\}. \end{aligned} \tag{11}$$

This is the disk of radius a centered at $R\hat{\boldsymbol{n}}$ and orthogonal to $\hat{\boldsymbol{n}}$, i.e. the disk of radius *a tangent to the sphere* S_R *at* $R\hat{\boldsymbol{n}}$. As $a \to 0$, $\mathcal{D}(\alpha\hat{\boldsymbol{n}})$ shrinks to the one-point set $\{R\hat{\boldsymbol{n}}\}$ and $\zeta_r \to \pm r_r$. We choose the branch with

$$\text{Re}\,\zeta_r \geqslant 0, \qquad \text{so that} \quad \zeta_r \to r_r \qquad \text{as} \quad a \to 0.$$

Define the real and imaginary parts of ζ_r by

$$\boxed{\zeta_r = \xi_r - \mathrm{i}\eta_r} \tag{12}$$

so that with our choice of branch,

$$\xi_r \geqslant 0 \qquad \text{and} \qquad \text{Sgn}\eta_r = \text{Sgn}(\boldsymbol{r}_r \cdot \hat{\boldsymbol{n}})$$

by (9). Since $w \leqslant 0$ on $\mathcal{D}(\alpha\hat{\boldsymbol{n}})$, ζ_r is imaginary there; hence, the branch cut can be characterized as

$$\mathcal{D}(\alpha\hat{\boldsymbol{n}}) = \{\boldsymbol{x}_r : \xi_r = 0\}. \tag{13}$$

Choosing cylindrical coordinates (ρ, ϕ, z) with the origin at $R\hat{\boldsymbol{n}}$ and the z-axis along $\hat{\boldsymbol{n}}$, (9) and (12) give

$$r_r^2 - a^2 = \xi_r^2 - \eta_r^2 \qquad \text{and} \qquad a\hat{\boldsymbol{n}} \cdot \boldsymbol{r}_r = a\mathrm{z} = \xi_r\eta_r;$$

hence,

$$a^2\rho^2 = a^2r_r^2 - a^2\mathrm{z}^2 = a^2\big(a^2 + \xi_r^2 - \eta_r^2\big) - \xi_r^2\eta_r^2 = \big(a^2 + \xi_r^2\big)\big(a^2 - \eta_r^2\big).$$

Thus, (ξ_r, η_r) are related to the cylindrical coordinates (ρ, z) by

$$\boxed{a\rho = \sqrt{a^2 + \xi_r^2}\sqrt{a^2 - \eta_r^2}, \qquad a\mathrm{z} = \xi_r\eta_r.} \tag{14}$$

This implies the following important inequalities:

$$-a \leqslant \eta_r \leqslant a \qquad \text{and} \qquad 0 \leqslant \xi_r \leqslant r_r, \tag{15}$$

where the second one follows from $\xi_r^2 = r_r^2 - \big(a^2 - \eta_r^2\big)$. Also by (14),

$$\frac{\rho^2}{a^2 + \xi_r^2} + \frac{\mathrm{z}^2}{\xi_r^2} = 1 \qquad \text{and} \qquad \frac{\rho^2}{a^2 - \eta_r^2} - \frac{\mathrm{z}^2}{\eta_r^2} = 1.$$

[5] We shall extend this idea to spacetime, where it applies, in particular, to solutions of the wave equation and Maxwell's equations.

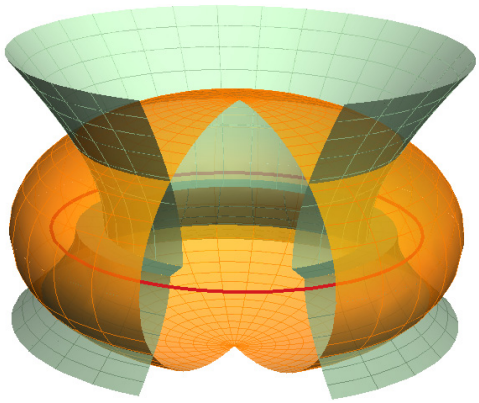

Figure 2. The real and imaginary parts of $\zeta_r = \xi_r - \mathrm{i}\eta_r$ form an oblate spheroidal coordinate system in $\mathbb{R}^3$ centered at $\boldsymbol{x}_r = R\hat{\boldsymbol{n}}$ with the z-axis along $\hat{\boldsymbol{n}}$. The third coordinate is ϕ, the standard azimuthal angle. The above plot shows cut-away views of an oblate spheroid $\mathcal{O}_{\xi_r}$ with $\xi_r = 0.7a$, a semi-hyperboloid $\mathcal{H}_{\eta_r}$ with $\eta_r = 0.8a$ ($z > 0$) and another with $\eta_r = -0.5a$ ($z < 0$). Also shown is the focal circle $\partial\mathcal{D}(\alpha\hat{\boldsymbol{n}})$ with radius a, whose interior is the branch disk $\mathcal{D}(\alpha\hat{\boldsymbol{n}})$.

This proves that the level surfaces of ξ_r and η_r are

$$\begin{aligned} \mathcal{O}_{\xi_r} &= \left\{ \boldsymbol{x}_r : \frac{\rho^2}{a^2 + \xi_r^2} + \frac{\mathrm{z}^2}{\xi_r^2} = 1 \right\}, \qquad \xi_r > 0 \\ \mathcal{H}_{\eta_r} &= \left\{ \boldsymbol{x}_r : \frac{\rho^2}{a^2 - \eta_r^2} - \frac{\mathrm{z}^2}{\eta_r^2} = 1,\ \mathrm{z}\eta_r \geqslant 0 \right\}, \qquad 0 < \eta_r^2 < a^2. \end{aligned} \tag{16}$$

The level surfaces of ξ_r are the *oblate spheroids* $\mathcal{O}_{\xi_r}$ and those of η_r are the *semi-hyperboloids* $\mathcal{H}_{\eta_r}$. The restriction $\mathrm{z}\eta_r \geqslant 0$ follows from $a\mathrm{z} = \xi_r\eta_r$ and $\xi_r > 0$. As $\xi_r \to 0$, $\mathcal{O}_{\xi_r}$ shrinks to the branch disk $\mathcal{D}(\alpha\hat{\boldsymbol{n}})$ (13). It can be shown [K3] that the families $\mathcal{O}_{\xi_r}$ and $\mathcal{H}_{\eta_r}$ are mutually orthogonal, forming an *oblate spheroidal coordinate system* deforming the spherical coordinates (r_r, θ_r, ϕ_r). They all share a common *focal circle*[6], which is the boundary of the branch disk:

$$\partial\mathcal{D}(\alpha\hat{\boldsymbol{n}}) = \{\boldsymbol{x}_r : r_r = a, \hat{\boldsymbol{n}} \cdot \boldsymbol{r}_r = 0\} = \{\boldsymbol{x}_r : \zeta_r = 0\}. \tag{17}$$

The last equality shows that $\partial\mathcal{D}(\alpha\hat{\boldsymbol{n}})$ is the set of all *branch points* of ζ_r. Whereas $f(w) = \sqrt{w}$ has a branch *point* at $w = 0$, $\zeta_r(\boldsymbol{x}_r) = \sqrt{(\boldsymbol{x}_r - \alpha\hat{\boldsymbol{n}})^2}$ has a branch *circle*. Figure 2 shows $\partial\mathcal{D}(\alpha\hat{\boldsymbol{n}})$ and examples of $\mathcal{O}_{\xi_r}$ and $\mathcal{H}_{\eta_r}$.

Since $(-\boldsymbol{z}_r)^2 = \boldsymbol{z}_r^2$, ζ_r is even as a function of $\boldsymbol{z}_r \in \mathbb{C}^3$. However, it is *not* even as a function of $\boldsymbol{r}_r$ alone. Instead, we have

$$\zeta_r(-\boldsymbol{r}_r - \mathrm{i}a\hat{\boldsymbol{n}}) = \zeta_r(\boldsymbol{r}_r + \mathrm{i}a\hat{\boldsymbol{n}}) = \zeta_r(\boldsymbol{r}_r - \mathrm{i}a\hat{\boldsymbol{n}})^*.$$

The last relation is a *reality condition* or *Hermiticity property* on the complex function $\zeta_r(\boldsymbol{z}_r)$, and it requires our choice of branch cut $\xi_r \geqslant 0$:

$$\zeta_r(\boldsymbol{z}_r^*) = \zeta_r(\boldsymbol{z}_r)^*. \tag{18}$$

We now use this to define the analytic continuation of r_e by

$$\zeta_e = \sqrt{(\boldsymbol{r}_e + \mathrm{i}a\hat{\boldsymbol{n}})^2} = (\sqrt{(\boldsymbol{r}_e - \mathrm{i}a\hat{\boldsymbol{n}})^2})^* = (\xi_e - \mathrm{i}\eta_e)^* = \xi_e + \mathrm{i}\eta_e.$$

[6] Its physical significance is that it consists entirely of focal points of both $\mathcal{O}_{\xi_r}$ and $\mathcal{H}_{\eta_r}$.

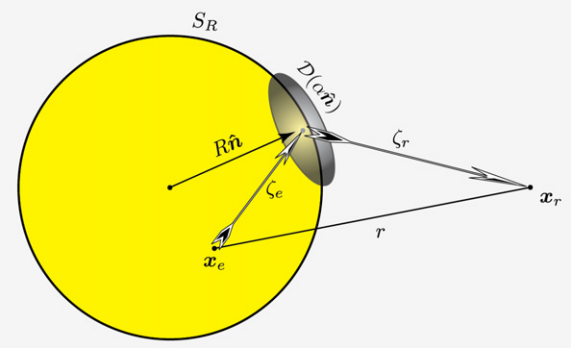

Figure 3. The complex point $\alpha\hat{\boldsymbol{n}}$ represents the real disk $\mathcal{D}(\alpha\hat{\boldsymbol{n}})$ tangent to the sphere S_R at $R\hat{\boldsymbol{n}}$. The complex distances ζ_e (from $\boldsymbol{x}_e$ to $\mathcal{D}(\alpha\hat{\boldsymbol{n}})$) and ζ_r (from $\mathcal{D}(\alpha\hat{\boldsymbol{n}})$ to $\boldsymbol{x}_r$) are depicted schematically, emphasizing their *directed* nature as explained in the text.

This shows that ζ_e and ζ_r are *directed* distances. Their sign difference indicates that $\alpha\hat{\boldsymbol{n}}$ is a *receiver* for the wave propagating from $\boldsymbol{x}_e$ and an *emitter* for the wave propagating to $\boldsymbol{x}_r$, as illustrated in figure 3. The sign difference is significant because the two sides of $\mathcal{D}(\alpha\hat{\boldsymbol{n}})$ have *opposite orientations*.

As functions of $\boldsymbol{x}_e$ for fixed $\alpha\hat{\boldsymbol{n}} \in \mathbb{C}^3$, ξ_e and η_e have the same properties as ξ_r and η_r except that the z-axis is now along $-\hat{\boldsymbol{n}}$ due to the opposite orientation of $\mathcal{D}(\alpha\hat{\boldsymbol{n}})$. For example, the level surfaces of ξ_e are oblate spheroids and those of η_e are semi-hyperboloids with

$$\xi_e \geqslant 0, \qquad \operatorname{Sgn}\eta_e = \operatorname{Sgn}(\hat{\boldsymbol{n}}\cdot\boldsymbol{r}_e).$$

However, it is clear from figure 1 that while η_r can have any value in $[-a, a]$, every emission point $\boldsymbol{x}_e$ in the interior of S_R must have

$$\hat{\boldsymbol{n}}\cdot\boldsymbol{r}_e > 0; \qquad \text{hence} \quad 0 < \eta_e \leqslant a.$$

It can be shown that the exact bounds on η_e as $\hat{\boldsymbol{n}}$ varies over S^2 are

$$\gamma a \leqslant \eta_e \leqslant a, \qquad \text{where} \quad \gamma = \sqrt{1 - \frac{|\boldsymbol{x}_e|^2}{|\alpha|^2}}. \tag{19}$$

It is clear that γ can depend only on $|\boldsymbol{x}_e|$ since the minimum of η_e must be spherically symmetric. In particular,

$$0 \leqslant |\boldsymbol{x}_e| < R \;\Rightarrow\; 0 < \gamma \leqslant 1, \qquad \gamma_0 \equiv \lim_{|\boldsymbol{x}_e|\to R}\gamma = \frac{a}{\sqrt{R^2+a^2}} < 1 \tag{20}$$

and

$$\boldsymbol{x}_e = \boldsymbol{0} \;\Rightarrow\; \eta_e = a \quad \text{for all } \hat{\boldsymbol{n}},$$

which is obvious since $\boldsymbol{x}_e = \boldsymbol{0} \;\Rightarrow\; \boldsymbol{z}_e = \alpha\hat{\boldsymbol{n}} \;\Rightarrow\; \zeta_e = \alpha \;\Rightarrow\; \xi_e = R,\ \eta_e = a$. The functions η_r and η_e will play an important role, and it is helpful to interpret them geometrically. From (16), it follows that $\mathcal{H}_{\eta_r}$ is asymptotic to the *cone* $\mathcal{C}_{\vartheta_r}$ making an angle ϑ_r with the positive z-axis and $\mathcal{H}_{\eta_e}$ is asymptotic to the cone $\mathcal{C}_{\vartheta_e}$ making an angle ϑ_e with the negative z-axis, where

$$a\cos\vartheta_r = \eta_r \qquad \text{and} \qquad a\cos\vartheta_e = \eta_e. \tag{21}$$

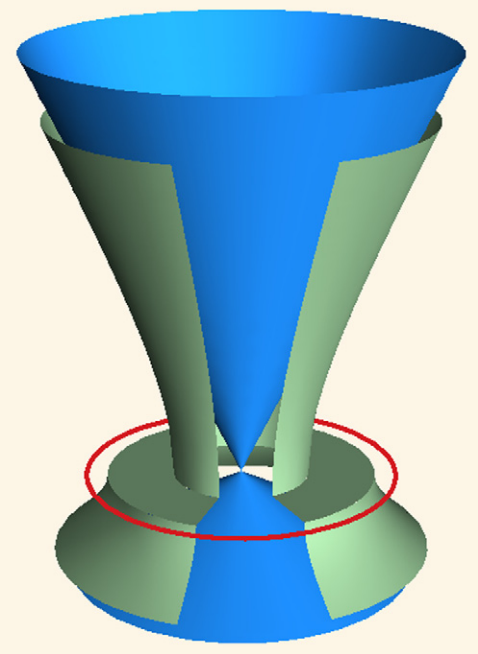

Figure 4. The semi-hyperboloids $\mathcal{H}_{\eta_r}$ (above) and $\mathcal{H}_{\eta_e}$ (below) for $\eta_r = 0.9a$ and $\eta_e = 0.5a$. Also shown are the asymptotic cones $\mathcal{C}_{\vartheta_r}$, $\mathcal{C}_{\vartheta_e}$ and the focal circle $\partial\mathcal{D}(\alpha\hat{\boldsymbol{n}})$. The cones make angles ϑ_r and ϑ_e with $\hat{\boldsymbol{n}}$ and $-\hat{\boldsymbol{n}}$, respectively, given by (21). The Huygens relation in the time domain will favor pulsed beams with $\eta_r > \eta_e$, which means that the wave is *focused* into narrower propagation hyperboloids $\mathcal{H}_{\eta_r}$ (asymptotic to the diffraction cones $\mathcal{C}_{\vartheta_r}$) upon being received along $\mathcal{H}_{\eta_e}$ and re-emitted by $\mathcal{D}(\alpha\hat{\boldsymbol{n}})$.

See figure 4. Hence, (19) can be restated as

$$\boxed{0 \leqslant \vartheta_e \leqslant \sin^{-1}\frac{|\boldsymbol{x}_e|}{|\alpha|},} \tag{22}$$

while $0 \leqslant \vartheta_r \leqslant \pi$.

The parameters ϑ_r, ϑ_e are deformations of the spherical coordinates θ_r, θ_e of $\boldsymbol{r}_r, \boldsymbol{r}_e$. A similar interpretation exists for ξ_r and ξ_e as deformations of the radial coordinates r_r, r_e: the oblate spheroid $\mathcal{O}_{\xi_r}$ containing $\boldsymbol{x}_r$ is tangent to the sphere S_{ξ_r} of radius ξ_r at the north and south poles, and the same goes for $\mathcal{O}_{\xi_e}$ and S_{ξ_e}; this explains why $\xi_r \leqslant r_r$ and $\xi_e \leqslant r_e$. These observations provide a complete *real* geometric interpretation of the complex distances ζ_r and ζ_e in $\mathbb{R}^3$. As an intuitive aid to understanding the idea, think of ζ_r as the 'distance' between the disk $\mathcal{D}(\alpha\hat{\boldsymbol{n}})$ and the point $\boldsymbol{x}_r$. Its complex nature reflects the fact that no single *real* number can characterize this distance, and that the distances from $\boldsymbol{x}_r$ to points on $\mathcal{D}(\alpha\hat{\boldsymbol{n}})$ depend on the inclination of the disk, which can be parameterized by ϑ_r or η_r. Hence, ζ_r is not spherically symmetric, like r_r, but cylindrically symmetric around $\hat{\boldsymbol{n}}$.

The functions ξ_r, η_r simplify if the observer is far from the disk:

$$\begin{aligned} r_r \gg a \Rightarrow\ & \zeta_r = \sqrt{r_r^2 - a^2 - 2\mathrm{i}a\boldsymbol{r}_r\cdot\hat{\boldsymbol{n}}} \sim r_r - \mathrm{i}a\hat{\boldsymbol{r}}_r\cdot\hat{\boldsymbol{n}} \\ \Rightarrow\ & \xi_r \sim r_r, \quad \eta_r \sim a\cos\theta_r \qquad \text{where} \quad \cos\theta_r \equiv \hat{\boldsymbol{r}}_r\cdot\hat{\boldsymbol{n}}. \end{aligned} \tag{23}$$

In particular, note that $\vartheta_r \sim \theta_r$ as expected. Hence, the spheroids $\mathcal{O}_{\xi_r}$ can be approximated by the spheres S_{r_r} and the semi-hyperboloids $\mathcal{H}_{\eta_r}$ by their asymptotic cones $\mathcal{C}_{\vartheta_r}$. The deformed variables (ξ_r, ϑ_r) are thus restored to their original values (r_r, θ_r). On the other hand, if the observer is far from the *sphere*, then

$$|\boldsymbol{x}_r| \gg R \;\Rightarrow\; r_r = |\boldsymbol{x}_r - R\hat{\boldsymbol{n}}| \sim |\boldsymbol{x}_r| - R\hat{\boldsymbol{x}}_r \cdot \hat{\boldsymbol{n}}.$$

The *far-zone approximation* assumes that the observer is far from both the disk and the sphere, which can be stated succinctly as follows:

$$|\boldsymbol{x}_r| \gg |\alpha| \;\Rightarrow\; \zeta_r = \sqrt{|\boldsymbol{x}_r|^2 + \alpha^2 - 2\alpha \boldsymbol{x}_r \cdot \hat{\boldsymbol{n}}} \sim |\boldsymbol{x}_r| - \alpha \hat{\boldsymbol{x}}_r \cdot \hat{\boldsymbol{n}}$$

or

$$|\boldsymbol{x}_r| \gg |\alpha| \;\Rightarrow\; \xi_r \sim r_r \sim |\boldsymbol{x}_r| - R\cos\theta_r \qquad \text{and} \qquad \eta_r \sim a\cos\theta_r. \tag{24}$$

In the engineering literature [N86], the set

$$S_\alpha = \{\alpha\hat{\boldsymbol{n}} \in \mathbb{C}^3 : \hat{\boldsymbol{n}} \in S^2\} \tag{25}$$

is called the *complex sphere*[7] of radius α in $\mathbb{C}^3$. The correspondence

$$\alpha\hat{\boldsymbol{n}} \in \mathbb{C}^3 \leftrightarrow \mathcal{D}(\alpha\hat{\boldsymbol{n}}) \subset \mathbb{R}^3 \tag{26}$$

establishes a complete equivalence between complex *points* and real *disks* (where a 'disk' with radius $a = 0$ is by definition a point). Under this equivalence, S_α corresponds to the set of all disks of radius a tangent to S_R, which is a *tangent disk bundle* with base S_R:

$$T_a(S_R) = \{\mathcal{D}(\alpha\hat{\boldsymbol{n}}) : \hat{\boldsymbol{n}} \in S^2\}, \qquad \alpha = R + \mathrm{i}a. \tag{27}$$

4. Generalized principle for time-harmonic waves

We can now continue (4) to complex space by extending (7) to

$$\begin{aligned} \tilde{G}_\omega(\boldsymbol{z}_e) &= \frac{\mathrm{e}^{\mathrm{i}\omega\zeta_e}}{\zeta_e}, \qquad \boldsymbol{z}_e = \alpha\hat{\boldsymbol{n}} - \boldsymbol{x}_e, \qquad \zeta_e = \sqrt{\boldsymbol{z}_e \cdot \boldsymbol{z}_e} \\ \tilde{G}_\omega(\boldsymbol{z}_r) &= \frac{\mathrm{e}^{\mathrm{i}\omega\zeta_r}}{\zeta_r}, \qquad \boldsymbol{z}_r = \boldsymbol{x}_r - \alpha\hat{\boldsymbol{n}}, \qquad \zeta_r = \sqrt{\boldsymbol{z}_r \cdot \boldsymbol{z}_r}. \end{aligned} \tag{28}$$

If the observer is far from the disk, (23) gives

$$r_r \gg a \;\Rightarrow\; \tilde{G}_\omega(\boldsymbol{z}_r) \sim \frac{\mathrm{e}^{\mathrm{i}\omega r_r}}{r_r}\,\mathrm{e}^{\omega a\cos\theta_r}, \tag{29}$$

where we have used $\zeta_r \sim r_r - \mathrm{i}a\cos\theta_r \sim r_r$ in the denominator. Thus $\tilde{G}_\omega$, viewed as a function of $\boldsymbol{r}_r \in \mathbb{R}^3$, has a *radiation pattern* [HY99]

$$\mathcal{F}_\omega(\theta_r) = \mathrm{e}^{\omega a\cos\theta_r}.$$

For $\omega > 0$, this is the pattern of a *beam propagating in the direction of* $\hat{\boldsymbol{n}}$, while for $\omega < 0$ the beam propagates in the direction of $-\hat{\boldsymbol{n}}$. The larger ωa,[8] the sharper the beam. Note further that these beams are very special in that they have *no sidelobes*. That makes them especially useful in applications such as communications and remote sensing. Analyticity in $\boldsymbol{z}_r$ combines with (2) to give

$$\left(\nabla_r^2 + \omega^2\right)\tilde{G}_\omega(\boldsymbol{x}_r - \alpha\hat{\boldsymbol{n}}) = 0 \qquad \text{when} \quad \boldsymbol{x}_r \notin \mathcal{D}(\alpha\hat{\boldsymbol{n}}), \tag{30}$$

[7] The term would be more appropriately applied to $\tilde{S}_\alpha = \{\boldsymbol{z} \in \mathbb{C}^3 : \boldsymbol{z}\cdot\boldsymbol{z} = \alpha^2\}$. Since S_α has real dimension 2 for $\alpha \neq 0$ while $\tilde{S}_\alpha$ has real dimension 4 (complex dimension 2), S_α is a proper subset of $\tilde{S}_\alpha$.

[8] Recall that $c = 1$, so $\omega a = ka = 2\pi a/\lambda$ where k is the wave number and λ is the wavelength. Thus, ωa can be interpreted as the *number of wavelengths in the circumference of* $\partial\mathcal{D}(\alpha\hat{\boldsymbol{n}})$.

where ∇_r^2 is the Laplacian with respect to $\boldsymbol{x}_r$. This proves that the disk $\mathcal{D}(\alpha\hat{\boldsymbol{n}})$ is the *source* of the beam. Just as the Huygens wavelet $G_\omega(\boldsymbol{x}_r - R\hat{\boldsymbol{n}})$ is radiated by a point source $\delta(\boldsymbol{x}_r - R\hat{\boldsymbol{n}})$ at $\boldsymbol{x}_r = R\hat{\boldsymbol{n}}$, as seen from (2), so is the beam $\tilde{G}_\omega(\boldsymbol{x}_r - \alpha\hat{\boldsymbol{n}})$ radiated by the branch disk $\mathcal{D}(\alpha\hat{\boldsymbol{n}})$. This will be made more precise later, in the time domain. In the limit $a \to 0$, $\tilde{G}_\omega(\boldsymbol{x}_r - \alpha\hat{\boldsymbol{n}})$ becomes the spherical wavelet $G_\omega(\boldsymbol{x}_r - R\hat{\boldsymbol{n}})$.

This method of deforming spherical time-harmonic waves to beams was first introduced by Deschamps [D71] and has become very popular in the engineering literature under the name *complex-source beams*, i.e. beams due *formally* to a 'point source' in $\mathbb{C}^3$, in our case $\alpha\hat{\boldsymbol{n}}$, but interpreted physically as a real disk [KS71, F76, C81, F82]. Solutions to scattering problems where the incident field is a complex-source beam are readily obtained by analytically continuing solutions with a spherical incident field [CH89]. Complex-point *receivers* were first introduced in [ZSB96] to model directed electroacoustic transducers in ultrasonics, and they have subsequently proven useful in cylindrical and spherical near-field scanning for both acoustic and electromagnetic fields [H6, H9, H9A].

An earlier application of complex distance was made in General Relativity by Ted Newman and his collaborators [NJ65, N65], who used it to give simple derivations of spinning black holes with and without charge (Kerr and Kerr–Newman solutions) by deforming known spherically symmetric solutions through analytic continuation[9].

However, none of the above works actually *compute* the source of $\tilde{G}_\omega$. This is not trivial because the singularities of $\tilde{G}_\omega$ on $\mathcal{D}(\alpha\hat{\boldsymbol{n}})$ are complicated by the branch cut: $\tilde{G}_\omega$ is infinite on the focal circle $\partial\mathcal{D}(\alpha\hat{\boldsymbol{n}})$, where $\zeta_r = 0$, and discontinuous on its interior. In [K3], the source $\tilde{\delta}_\omega$ of $\tilde{G}_\omega$ is *defined* by extending (2) and (30) to

$$4\pi\tilde{\delta}_\omega(\boldsymbol{x}_r - \alpha\hat{\boldsymbol{n}}) \equiv -\big(\nabla_r^2 + \omega^2\big)\tilde{G}_\omega(\boldsymbol{x}_r - \alpha\hat{\boldsymbol{n}}), \tag{31}$$

where ∇_r^2 is the *distributional* Laplacian with respect to $\boldsymbol{x}_r$. It is proved that $\tilde{\delta}_\omega$ is a generalized function supported on $\boldsymbol{x}_r \in \mathcal{D}(\alpha\hat{\boldsymbol{n}})$. In [K4a], it is shown that the analytically continued Coulomb potential

$$\tilde{\Phi} = \frac{1}{\zeta}, \qquad \boldsymbol{z} = \boldsymbol{x} - \mathrm{i}\boldsymbol{a} \in \mathbb{C}^3, \qquad \zeta = \sqrt{\boldsymbol{z}\cdot\boldsymbol{z}}$$

generates a *real* electromagnetic field $(\boldsymbol{E}, \boldsymbol{H})$ in the complex-analytic form

$$-\nabla\tilde{\Phi} = \boldsymbol{E} + \mathrm{i}\boldsymbol{H},$$

which in turn identifies its source $\mathcal{D}(\boldsymbol{a})$ as a spinning charged disk whose boundary moves at the speed of light. This is the flat-space version of the Kerr–Newman black hole, studied from a different viewpoint by Newman in [N73]. This analysis is generalized to higher dimensions in [K0], where a rigorous connection between solutions of Laplace's equation in $\mathbb{R}^{n+1}$ and the wave equation in $\mathbb{R}^{n,1}$ (Minkowski space with n space dimensions plus time) is established, generalizing earlier work by Garabedian [G64].

We are now ready to state and prove the analytic Huygens principle for time-harmonic waves.

Theorem 1. *For given emission and reception points $\boldsymbol{x}_e$, $\boldsymbol{x}_r$ with $|\boldsymbol{x}_e| < |\boldsymbol{x}_r|$, the Huygens reproducing relation (5) extends analytically to complex R in the open set*

$$A = \{\alpha \in \mathbb{C} : \mathrm{Re}\,\alpha > |\boldsymbol{x}_e|,\ |\alpha| < |\boldsymbol{x}_r|\}, \qquad \alpha = R + \mathrm{i}a. \tag{32}$$

[9] The first derivation of a cylindrically symmetric solution of Einstein's equation was given by Roy Kerr in 1963 [K63]. It was very complicated, which explains why it had taken 48 years to generalize Karl Schwarzschild's spherical solution. Newman's derivation, based on the complex distance, was a model of simplicity.

For $\alpha \in A$, it states that

$$G_\omega(\boldsymbol{x}_r - \boldsymbol{x}_e) = -\frac{\alpha^2}{4\pi} \int \mathrm{d}\hat{\boldsymbol{n}} \tilde{G}_\omega(\boldsymbol{x}_r - \alpha\hat{\boldsymbol{n}}) \overleftrightarrow{\partial}_\alpha \tilde{G}_\omega(\alpha\hat{\boldsymbol{n}} - \boldsymbol{x}_e) \tag{33}$$

or

$$\frac{\mathrm{e}^{\mathrm{i}\omega r}}{r} = -\frac{\alpha^2}{4\pi} \int \mathrm{d}\hat{\boldsymbol{n}} \frac{\mathrm{e}^{\mathrm{i}\omega\zeta_r}}{\zeta_r} \overleftrightarrow{\partial}_\alpha \frac{\mathrm{e}^{\mathrm{i}\omega\zeta_e}}{\zeta_e}, \qquad r = |\boldsymbol{x}_r - \boldsymbol{x}_e|. \tag{34}$$

Proof. Write (33) as

$$\mathcal{L} = \mathcal{R}(\alpha),$$

where the left-hand side $\mathcal{L}$ is independent of α as noted. This reduces to (5) for $\alpha = R$ with $|\boldsymbol{x}_e| < R < |\boldsymbol{x}_r|$. The right-hand side $\mathcal{R}(\alpha)$ is analytic as long as neither $\boldsymbol{x}_e$ nor $\boldsymbol{x}_r$ belongs to any of the branch disks $\mathcal{D}(\alpha\hat{\boldsymbol{n}})$. But the union of all these branch disks is the spherical shell

$$S_R^a = \bigcup_{\hat{\boldsymbol{n}} \in S^2} \mathcal{D}(\alpha\hat{\boldsymbol{n}}) = \{\boldsymbol{x} \in \mathbb{R}^3 : \ R \leqslant |\boldsymbol{x}| \leqslant \sqrt{R^2 + a^2} = |\alpha|\}; \tag{35}$$

hence, $\boldsymbol{x}_e$ must be in the interior of S_R^a and $\boldsymbol{x}_r$ in its exterior. This means that $\mathcal{R}(\alpha)$ is analytic in A, and since it is constant on the line segment $A \cap \mathbb{R}$, it must be constant throughout A. □

Equation (33) can be interpreted physically as follows: $\tilde{G}_\omega(\alpha\hat{\boldsymbol{n}} - \boldsymbol{x}_e)$ is the *reception amplitude* by the disk $\mathcal{D}(\alpha\hat{\boldsymbol{n}})$ of the wave emitted by $\boldsymbol{x}_e$, which in turn stimulates the *emission* of the complex-source beam $\tilde{G}_\omega(\boldsymbol{x}_r - \alpha\hat{\boldsymbol{n}})$ propagating to $\boldsymbol{x}_r$. The spherical wave $G_\omega(\boldsymbol{x}_r - \boldsymbol{x}_e)$ from $\boldsymbol{x}_e$ to $\boldsymbol{x}_r$ is thus represented as a sum of beams.

Equation (34) can be further simplified by letting

$$\zeta_e(\alpha) = \sqrt{(\alpha\hat{\boldsymbol{n}} - \boldsymbol{x}_e)^2} \qquad \text{and} \qquad \zeta_r(\alpha') = \sqrt{(\boldsymbol{x}_r - \alpha'\hat{\boldsymbol{n}})^2} \tag{36}$$

with α and α' independent. Then,

$$\boxed{\frac{\mathrm{e}^{\mathrm{i}\omega r}}{r} = \frac{\alpha^2}{4\pi} \partial_{\alpha'\alpha} \int \frac{\mathrm{d}\hat{\boldsymbol{n}}}{\zeta_r \zeta_e} \mathrm{e}^{\mathrm{i}\omega(\zeta_r + \zeta_e)},} \tag{37}$$

where

$$\partial_{\alpha'\alpha} = \{\partial_{\alpha'} - \partial_\alpha\}|_{\alpha'=\alpha}.$$

Applying the derivatives gives a version of (37) more suitable for numerical computations:

$$\frac{\mathrm{e}^{\mathrm{i}\omega r}}{r} = \frac{\alpha^2}{4\pi} \int \frac{\mathrm{d}\hat{\boldsymbol{n}}}{\zeta_r \zeta_e} \left[i\omega(\zeta_r' - \zeta_e') - \frac{\zeta_r'}{\zeta_r} + \frac{\zeta_e'}{\zeta_e} \right] \mathrm{e}^{\mathrm{i}\omega(\zeta_r + \zeta_e)}, \tag{38}$$

where

$$\zeta_e' \equiv \partial_\alpha \zeta_e = \frac{\alpha - \hat{\boldsymbol{n}} \cdot \boldsymbol{x}_e}{\zeta_e}, \qquad \zeta_r' \equiv \partial_{\alpha'} \zeta_r = \frac{\alpha' - \hat{\boldsymbol{n}} \cdot \boldsymbol{x}_r}{\zeta_r}. \tag{39}$$

Let us note a symmetry of (37). Since the left-hand side satisfies the Fourier transform reality condition $\hat{f}(-\omega)^* = \hat{f}(\omega)$, so must the right-hand side; thus,

$$\frac{\mathrm{e}^{\mathrm{i}\omega r}}{r} = \frac{\alpha^{*2}}{4\pi} \partial_{\alpha'^*\alpha^*} \int \frac{\mathrm{d}\hat{\boldsymbol{n}}}{\zeta_r^* \zeta_e^*} \mathrm{e}^{\mathrm{i}\omega(\zeta_r^* + \zeta_e^*)}. \tag{40}$$

The branches defined by $\operatorname{Re} \zeta_e \geqslant 0$ and $\operatorname{Re} \zeta_r \geqslant 0$ satisfy the reality conditions (18)

$$\zeta_e(\alpha)^* = \zeta_e(\alpha^*) \qquad \text{and} \qquad \zeta_r(\alpha')^* = \zeta_r(\alpha'^*);$$

hence, the right-hand side of (40) is simply (37) with $\alpha \to \alpha^*$ and $\alpha' \to \alpha'^*$. Since the set A (32) is symmetric under complex conjugation, this explains why (40) and (37) are consistent. That is, the right-hand side of (37) satisfies the *extended* reality condition

$$\hat{f}(-\omega, \alpha^*)^* = \hat{f}(\omega, \alpha). \tag{41}$$

Equation (33) implies that the field radiated by an arbitrary source $\varrho_\omega(\boldsymbol{x}_e)$ supported in S_R is

$$F_\omega(\boldsymbol{x}_r) = \frac{\alpha^2}{4\pi} \partial_{\alpha'\alpha} \int \mathrm{d}\hat{\boldsymbol{n}} \tilde{G}_\omega(\boldsymbol{x}_r - \alpha'\hat{\boldsymbol{n}}) \tilde{F}_\omega(\alpha\hat{\boldsymbol{n}}), \tag{42}$$

where

$$\tilde{F}_\omega(\alpha\hat{\boldsymbol{n}}) = \int \mathrm{d}\boldsymbol{x}_e \tilde{G}_\omega(\alpha\hat{\boldsymbol{n}} - \boldsymbol{x}_e) \varrho_\omega(\boldsymbol{x}_e) \tag{43}$$

is the analytic continuation of the radiated field $F_\omega(R\hat{\boldsymbol{n}})$ from S_R to S_α. $\tilde{F}_\omega(\alpha\hat{\boldsymbol{n}})$ can be interpreted as the *reception amplitude* of the radiation field by the disk $\mathcal{D}(\alpha\hat{\boldsymbol{n}})$ [ZSB96]. See also section 10, where this is proved in the time domain using a rigorous definition of pulsed-beam sources. Thus, (42) has a simple physical interpretation: the field radiated by ϱ_ω is *intercepted by* $\mathcal{D}(\alpha\hat{\boldsymbol{n}})$ *and re-radiated by* $\mathcal{D}(\alpha'\hat{\boldsymbol{n}})$ to give an identical field in the exterior, showing that ϱ_ω can be replaced by an equivalent source on the tangent disk bundle $T_a(S_R)$ given in (27).

Equation (42) gives the field radiated by ϱ_ω as a superposition of the complex-source beams $\tilde{G}_\omega(\boldsymbol{x}_r - \alpha\hat{\boldsymbol{n}})$ with source points $\alpha\hat{\boldsymbol{n}} \in S_\alpha$. The first exact representation of this type was obtained by Norris [N86], who expressed the field of a single real point source at the *origin* in terms of complex-source beams emanating from a sphere centered at the origin. Heyman [H89] translated Norris' result into the time domain using the analytic-signal (positive-frequency) Fourier transform. Norris and Hansen subsequently generalized the result to arbitrary bounded sources, both in the frequency domain [NH97] and time domain [HN97].

However, the representations [NH97, HN97] are very different from (42). They express the *weights* of the complex-source beams in terms of the spherical-harmonic expansion coefficients of ϱ_ω, which requires only the field and not its normal derivative. On the other hand, since each of these coefficients involves an integration of the field over the entire sphere, it is not possible to express the weight of the complex-source beam emanating from $\alpha\hat{\boldsymbol{n}}$ in terms of the incident field at that point, as in (42). Hence, the expansions in [NH97] and [HN97] are *nonlocal*, and consequently they do not have a straightforward physical interpretation like the one above.

An electromagnetic analog of (42) has been published in [TPB7] and used in [TPB7A] to accelerate the method of moments.

The representations (33) and (42) can be further generalized to surfaces S other than spheres. It need not even be assumed that the source disks represented by the points of the analytically continued surface $\tilde{S}$ must be tangent to S. However, this more general analytic continuation is more difficult than extending a single parameter like R. It does not work for all 'regular' surfaces[10] for which a real Huygens representation holds because the integral expression is not necessarily analytic in a sufficiently large domain. To obtain an analytic continuation for a surface S, it is necessary to ensure that (a) the integration avoids all branch cuts, and (b) the area measure of S, which involves a Jacobian, can be continued analytically. These topics will be considered in future work.

[10] A *regular* surface is defined by Kellogg [K67]; see also [HY99, chapter 2].

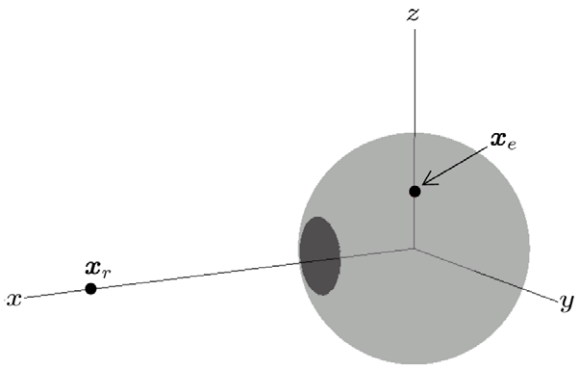

Figure 5. Decomposition (47) with $R = 5, a = 1, \boldsymbol{x}_e = (0, 0, 2.5), \boldsymbol{x}_r = (20, 0, 0)$. The dark region (closest to $\boldsymbol{x}_r$) is S_R^+ and the light region is S_R^-.

5. Generalized principle in the time domain

Care must be taken when transforming (37) to the time domain because the integrand can grow exponentially in ω. Letting

$$\zeta = \zeta_r + \zeta_e = \xi - \mathrm{i}\eta, \qquad \xi = \xi_r + \xi_e, \qquad \eta = \eta_r - \eta_e, \tag{44}$$

the exponential in (37) is

$$\mathrm{e}^{\mathrm{i}\omega\zeta} = \mathrm{e}^{\mathrm{i}\omega\xi}\,\mathrm{e}^{\omega\eta}. \tag{45}$$

Setting $\alpha' = \alpha$ (as it will be after applying $\partial_{\alpha'\alpha}$), (19) shows that the bounds on η, as $\hat{\boldsymbol{n}}$ varies with $\boldsymbol{x}_e$ fixed, are

$$-2a \leqslant \eta \leqslant (1-\gamma)a \qquad \text{where} \quad \gamma = \sqrt{1 - \frac{|\boldsymbol{x}_e|^2}{R^2 + a^2}}. \tag{46}$$

The upper bound of η is therefore positive whenever $\boldsymbol{x}_e \neq \boldsymbol{0}$. This divides the sphere S_R into the subsets

$$S_R^+(\boldsymbol{x}_e, \boldsymbol{x}_r) = \{R\hat{\boldsymbol{n}} : \eta_r > \eta_e\}, \qquad S_R^-(\boldsymbol{x}_e, \boldsymbol{x}_r) = \{R\hat{\boldsymbol{n}} : \eta_r \leqslant \eta_e\} \tag{47}$$

shown in figure 5.

As indicated, these sets depend on $\boldsymbol{x}_e$ and $\boldsymbol{x}_r$. We call S_R^+ the *frontal zone* and S_R^- the *rear zone* of S_R for the given emission and reception points $\boldsymbol{x}_e, \boldsymbol{x}_r$. Note that the *maximal* value $\eta_e = a$ is attained when $\boldsymbol{x}_e$ is in the direction of $-\hat{\boldsymbol{n}}$, i.e.

$$\eta_e = a \;\Rightarrow\; \boldsymbol{x}_e = -|\boldsymbol{x}_e|\hat{\boldsymbol{n}}, \tag{48}$$

which gives the *weakest* contribution. This is a result of the opposite orientations of the reception and emission disks.

To obtain the time-domain version of (37) choose a signal $g(t)$, multiply both sides by $\hat{g}(\omega)$ and take the inverse Fourier transform. Formally, this gives

$$\frac{g(t-r)}{r} = \frac{\alpha^2}{8\pi^2}\partial_{\alpha'\alpha}\int \frac{\mathrm{d}\hat{\boldsymbol{n}}}{\zeta_r\zeta_e}\int_{-\infty}^{\infty}\mathrm{d}\omega\,\mathrm{e}^{-\mathrm{i}\omega(t-\zeta)}\hat{g}(\omega), \tag{49}$$

where we have exchanged the order of integration on the right-hand side, which is justified if the double integral converges absolutely. If g is real, it suffices to compute its positive-frequency component and then take the real part. The positive-frequency component of $g(t)$ is called its *analytic signal:*

$$\tilde{g}(t) = \frac{1}{2\pi}\int_0^{\infty}\mathrm{d}\omega\,\mathrm{e}^{-\mathrm{i}\omega t}\hat{g}(\omega), \qquad \hat{\tilde{g}}(\omega) = H(\omega)\hat{g}(\omega), \tag{50}$$

where $H(\omega)$ is the Heaviside step function. Taking the complex conjugate and using the reality condition $\hat{g}(\omega)^* = \hat{g}(-\omega)$ gives the negative-frequency component,

$$\tilde{g}(t)^* = \frac{1}{2\pi}\int_0^\infty \mathrm{d}\omega\, \mathrm{e}^{\mathrm{i}\omega t}\hat{g}(-\omega) = \frac{1}{2\pi}\int_{-\infty}^0 \mathrm{d}\omega\, \mathrm{e}^{-\mathrm{i}\omega t}\hat{g}(\omega);$$

hence,

$$g(t) = 2\,\mathrm{Re}\,\tilde{g}(t). \tag{51}$$

If $\hat{g}(\omega)$ decays sufficiently rapidly as $\omega \to \infty$, then the integral

$$\tilde{g}(\tau) = \frac{1}{2\pi}\int_0^\infty \mathrm{d}\omega\, \mathrm{e}^{-\mathrm{i}\omega\tau}\hat{g}(\omega), \qquad \tau = t + \mathrm{i}s \tag{52}$$

defines an analytic function of the complex time τ. The domain of analyticity depends on the decay properties of $\hat{g}$. Formally, the positive-frequency part of (49) is therefore

$$\frac{\tilde{g}(t-r)}{r} = \frac{\alpha^2}{4\pi}\partial_{\alpha'\alpha}\int \frac{\mathrm{d}\hat{\boldsymbol{n}}}{\zeta_r\zeta_e}\tilde{g}(t-\zeta) \tag{53}$$

provided the integral (52) defining $\tilde{g}(t-\zeta)$ converges absolutely for all $\hat{\boldsymbol{n}}$. Of special interest is the *impulse*

$$g(t) = \delta(t) \;\Rightarrow\; \hat{g}(\omega) \equiv 1 \;\Rightarrow\; \tilde{g}(\tau) = \frac{1}{2\pi\mathrm{i}\tau}, \qquad s < 0.$$

The integral converges to the *Cauchy kernel* for $s < 0$ and diverges for $s > 0$. The choice $g(t) = \delta(t)$ is very attractive since

$$\frac{\delta(t-r)}{r} \equiv P(\boldsymbol{x}, t) \tag{54}$$

is the *retarded wave propagator*, the unique *causal fundamental solution* of the wave equation:

$$\Box\, P(x) \equiv (\partial_t^2 - \nabla^2)P(x) = 4\pi\delta(x), \qquad x = (\boldsymbol{x}, t), \tag{55}$$

where P represents the wave radiated by the point source $\delta(x)$ at the origin of spacetime. It is 'fundamental' because it generates the field radiated by a general source ϱ through

$$F(x_r) = \int \mathrm{d}^4x_e\, P(x_r - x_e)\varrho(x_e) \;\Rightarrow\; \Box\, F(x) = 4\pi\varrho(x). \tag{56}$$

Thus, if we could obtain a pulsed-beam expansion for P, this would immediately give a similar expansion for all radiation fields F. However, it turns out that the divergence of (52) for $s > 0$ makes this task very difficult. Equation (53) requires

$$\tilde{g}(t-\zeta) = \tilde{g}(t - \xi + \mathrm{i}\eta)$$

both when $\eta_r \leqslant \eta_e$ and when $\eta_r > \eta_e$. Numerical experiments have shown that while (53) 'almost' works with the Cauchy kernel, there is always a small but critical *failure interval* $T = [t_1, t_2]$ where it fails to converge.

Note that disks are ideal for radiating *beams* (hence we have dish antennas) and recall that each point on S_R represents a tangent disk of radius a. Thus it is reasonable to try constructing a *compressed* representation of radiation fields by *boosting* contributions from the frontal zone S_R^+, where $\eta_r > \eta_e$, and *suppressing* contributions from the rear zone S_R^-, where $\eta_r \leqslant \eta_e$. The main contributions to (53) then come from the frontal zone, and this justifies the name 'compression.'

However, the Cauchy kernel does this *too* well: it not only boosts contributions from the frontal zone, but makes them *infinite*, thus destroying our representation. We shall solve this problem with an elegant *regularization* which behaves naturally with respect to spacetime

convolutions. This is very important because Huygens' principle is based on spacetime convolutions, as we shall see. Let

$$g_d(t) = \frac{\mathrm{e}^{-t^2/d^2}}{\sqrt{\pi}\, d}, \qquad d > 0. \tag{57}$$

This is the Gaussian distribution with standard deviation $\sigma = d/\sqrt{2}$. Although it seems that generality is lost by specializing to g_d, this is actually not the case because

$$d \to 0 \;\Rightarrow\; g_d(t) \to \delta(t). \tag{58}$$

Therefore, every continuous signal can be expressed as the limit of a superposition of translated versions of g_d:

$$g(t) = \lim_{d\to 0} \int_{-\infty}^{\infty} \mathrm{d}t' g(t') g_d(t - t').$$

In this sense, $g_d(t)$ and its translates form a generalized 'basis' for signals. Define the *Gaussian wave propagator*

$$P_d(x) = \frac{g_d(t - r)}{r}, \qquad x = (\boldsymbol{x}, t), \qquad r = |\boldsymbol{x}|. \tag{59}$$

By (58), P_d converges to the retarded wave propagator as $d \to 0$:

$$\lim_{d\to 0} P_d(x) = \frac{\delta(t - r)}{r} = P(x). \tag{60}$$

Its source is a 'Gaussianized' version of $\delta(x)$:

$$\Box\, P_d(x) = 4\pi g_d(t)\delta(\boldsymbol{x}) \equiv 4\pi \delta_d(x), \qquad \lim_{d\to 0} \delta_d(x) = \delta(x). \tag{61}$$

Just as P generates all radiation fields F by (56), so does P_d generate their Gaussianized versions:

$$F_d(x_r) \equiv \int \mathrm{d}^4 x_e P_d(x_r - x_e)\varrho(x_e), \qquad \lim_{d\to 0} F_d(x) = F(x), \tag{62}$$

whose source is a Gaussianized version ϱ_d of ϱ:

$$\Box\, F_d(x) = 4\pi \int \mathrm{d}^4 x_e \delta_d(x_r - x_e)\varrho(x_e) \equiv 4\pi \varrho_d(x), \qquad \lim_{d\to 0} \varrho_d(x) = \varrho(x).$$

The Fourier transform of $g_d(t)$ is

$$\hat{g}_d(\omega) = \mathrm{e}^{-d^2\omega^2/4};$$

thus,

$$g_d(t) = \frac{1}{2\pi} \int_{-\infty}^{\infty} \mathrm{d}\omega\, \mathrm{e}^{-\mathrm{i}\omega t}\, \mathrm{e}^{-d^2\omega^2/4}. \tag{63}$$

Both sides extend analytically to the whole complex time plane, giving a Fourier representation of the entire-analytic function $g_d(\tau)$:

$$\begin{aligned} \frac{1}{2\pi}\int_{-\infty}^{\infty} \mathrm{d}\omega\, \mathrm{e}^{-\mathrm{i}\omega\tau}\, \mathrm{e}^{-d^2\omega^2/4} &= \frac{\mathrm{e}^{-\tau^2/d^2}}{2\pi}\int_{-\infty}^{\infty} \mathrm{d}\omega\, \mathrm{e}^{-(d\omega/2+\mathrm{i}\tau/d)^2} \\ &= \frac{\mathrm{e}^{-\tau^2/d^2}}{\sqrt{\pi} d} = g_d(\tau). \end{aligned}$$

The positive-frequency part of g_d is

$$\tilde{g}_d(\tau) = \frac{1}{2\pi} \int_0^{\infty} \mathrm{d}\omega\, \mathrm{e}^{-\mathrm{i}\omega\tau}\, \mathrm{e}^{-d^2\omega^2/4} = \frac{\mathrm{e}^{-\tau^2/d^2}}{2\pi} \int_0^{\infty} \mathrm{d}\omega\, \mathrm{e}^{-(d\omega/2+\mathrm{i}\tau/d)^2}. \tag{64}$$

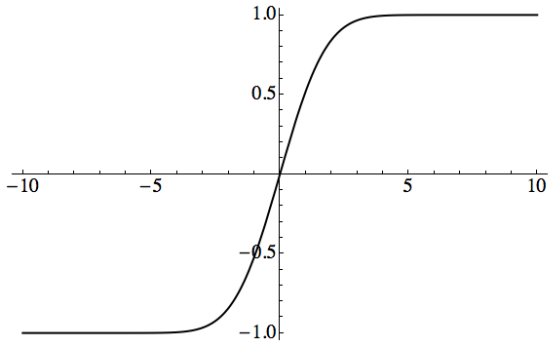

Figure 6. The error function $\operatorname{erf}(s/d)$, here plotted with $d = 2$, is a smoothed version of $\operatorname{Sgn} s$ to order d. As $d \to 0$, $\operatorname{erf}(s/d) \to \operatorname{Sgn}(s)$.

Thus,

$$\tilde{g}_d(\tau) = \frac{1}{2}\operatorname{erfc}(\mathrm{i}\tau/d)g_d(\tau) = \frac{w(-\tau/d)}{2\sqrt{\pi}d}, \tag{65}$$

where

$$\operatorname{erfc}(\mathrm{i}\tau/d) = \frac{2}{\sqrt{\pi}}\int_{i\tau/d}^{\infty} \mathrm{d}u\, \mathrm{e}^{-u^2} = 1 - \operatorname{erf}(\mathrm{i}\tau/d)$$

is the *complementary error function* and w is the *Faddeeva function* [AS70]. Since both g_d and erfc are entire, so is $\tilde{g}_d$. Define the function

$$\tilde{H}_d(s - \mathrm{i}t) = \tilde{H}_d(-\mathrm{i}\tau) \equiv \frac{1}{2}\operatorname{erfc}(\mathrm{i}\tau/d),$$

so that

$$\boxed{\tilde{g}_d(\tau) = \tilde{H}_d(-\mathrm{i}\tau)g_d(\tau).} \tag{66}$$

As illustrated in figure 6, $\operatorname{erf}(s/d)$ is a smoothed version of $\operatorname{Sgn}(s)$:

$$\operatorname{erf}(s/d) \equiv \frac{2}{\sqrt{\pi}}\int_0^{s/d} \mathrm{d}u\, \mathrm{e}^{-u^2} \sim \operatorname{Sgn}(s), \qquad \lim_{d\to 0}\operatorname{erf}(s/d) = \operatorname{Sgn}(s)$$

and the smoothing is of order d, meaning that

$$s < -d \;\Rightarrow\; \operatorname{erf}(s/d) \approx -1 \qquad \text{and} \qquad s > d \;\Rightarrow\; \operatorname{erf}(s/d) \approx 1.$$

Since

$$\frac{1 + \operatorname{Sgn}(s)}{2} = H(s) = \begin{cases} 1, & s > 0 \\ 0, & s < 0 \end{cases}$$

is the Heaviside step function and

$$2\tilde{H}_d(s - \mathrm{i}t) = 1 - \operatorname{erf}(\mathrm{i}\tau/d) = 1 + \operatorname{erf}((s - \mathrm{i}t)/d),$$

$\tilde{H}_d(s - \mathrm{i}t)$ is the analytic continuation of a smoothed version of $H(s)$ with

$$\lim_{d\to 0}\tilde{H}_d(s) \to H(s).$$

Again the smoothing is of order d:

$$s \leqslant -d \quad \Rightarrow \quad \tilde{H}_d(s) \approx 0 \qquad \text{and} \qquad s \geqslant d \quad \Rightarrow \quad \tilde{H}_d(s) \approx 1. \tag{67}$$

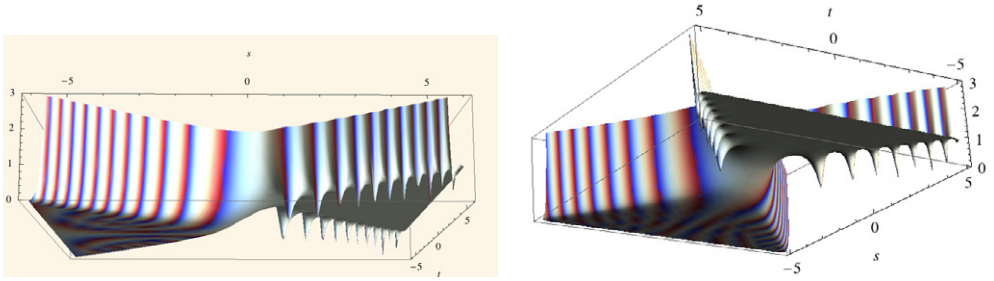

Figure 7. Plot of $|\tilde{H}_d(s - \mathrm{i}t)|$, shown from the side (left) and from below (right), where it is seen to be an approximation to a smoothed version of $H(s)$ for $|s| > |t|$ and have exponential growth for $|t| > |s|$. The smoothing is of order d and the spikes along $s = |t|$ are zeros. The phase of $\tilde{H}_d$ is color-coded on the surface representing its modus.

For small d, $|\tilde{H}_d(s - \mathrm{i}t)|$ is remarkably close to $H(s)$ when $|s| > |t|$. This can be seen in figure 7.[11]

Furthermore, since

$$\operatorname{erf}(\mathrm{i}\tau/d) + \operatorname{erf}(-\mathrm{i}\tau/d) \equiv 0 \;\Rightarrow\; \operatorname{erfc}(\mathrm{i}\tau/d) + \operatorname{erfc}(-\mathrm{i}\tau/d) \equiv 2,$$

$\tilde{H}_d$ extends analytically the *partitioning property* $H(s) + H(-s) \equiv 1$:

$$\tilde{H}_d(-\mathrm{i}\tau) + \tilde{H}_d(\mathrm{i}\tau) \equiv 1. \tag{68}$$

Since $g_d(\tau)$ is even, (66) and (68) imply

$$\tilde{g}_d(\tau) + \tilde{g}_d(-\tau) = g_d(\tau). \tag{69}$$

But

$$g_d(t + \mathrm{i}s) = \frac{\mathrm{e}^{(s^2-t^2)/d^2}}{\sqrt{\pi}\, d}\, \mathrm{e}^{-2\mathrm{i}st/d^2} = g_d(t)\, \mathrm{e}^{s^2/d^2}\, \mathrm{e}^{-2\mathrm{i}st/d^2}; \tag{70}$$

hence, $g_d(t + \mathrm{i}s)$ grows exponentially when $|s| > |t|$ and decays exponentially when $|t| > |s|$. The factor $\tilde{H}_d(-\mathrm{i}\tau)$ in (66) suppresses the negative cone $s < -|t|$, thus making $\tilde{g}_d(t + \mathrm{i}s)$ small everywhere outside the positive cone $s > |t|$. This is illustrated in figure 8.

More precisely, the continuous-fraction expression [AS70, 7.1.4] for erfc implies that

$$|\tau| \to \infty, \qquad s < 0 \;\Rightarrow\; \tilde{g}_d(\tau) \sim \frac{1}{2\pi\mathrm{i}\tau};$$

hence, by (69)

$$|\tau| \to \infty, \qquad s < 0 \;\Rightarrow\; \tilde{g}_d(-\tau) \sim g_d(\tau) - \frac{1}{2\pi\mathrm{i}\tau}.$$

The substitution $\tau \to -\tau$ gives

$$|\tau| \to \infty, \qquad s > 0 \;\Rightarrow\; \tilde{g}_d(\tau) \sim g_d(\tau) + \frac{1}{2\pi\mathrm{i}\tau},$$

and the two estimates can be combined into one that will be very useful[12],

$$\boxed{|\tau| \to \infty \;\Rightarrow\; \tilde{g}_d(\tau) \sim H(s) g_d(\tau) + \frac{1}{2\pi\mathrm{i}\tau}.} \tag{71}$$

[11] We thank David Park for generating this very informative plot using his *Presentations* Package for Mathematica http://home.comcast.net/-djmpark/Mathematica.html.

[12] Equation (71) is valid for $s = 0$, since $g_d(t) \to 0$ as $|t| \to \infty$.

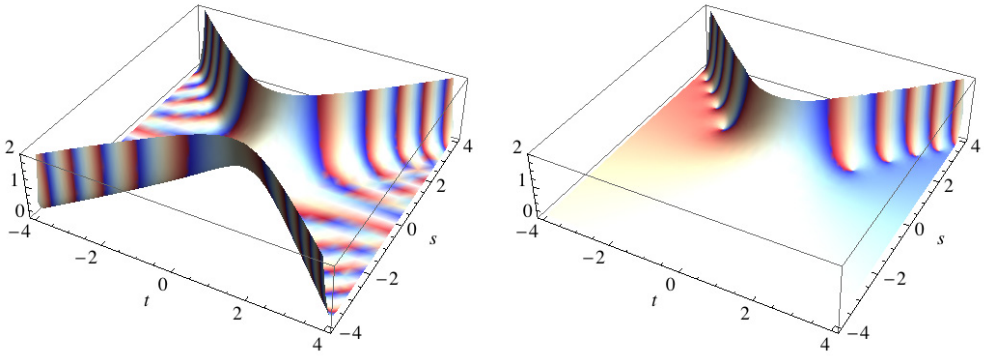

Figure 8. Plots of $|g_d(t+\mathrm{i}s)|$ (left) and $|\tilde{g}_d(t+\mathrm{i}s)|$ (right) with $d=1$. g_d grows exponentially in the double cone $|s|>|t|$ and decays exponentially in the double cone $|t|>|s|$, while $\tilde{g}_d$ grows exponentially in the single cone $s>|t|$ and decays elsewhere. The dimples in $\tilde{g}_d$ are zeros of $\operatorname{erfc}(\mathrm{i}\tau/d)$ (see figure 7) and the phases of g_d and $\tilde{g}_d$ are color-coded on the surfaces representing their moduli (see footnote 11). This shows the oscillation at the compression frequency (83) in the plot of $g_d(\tau)$ and its perturbed version (due to the complex factor $\tilde{H}_d(-\mathrm{i}\tau)$) in the plot of $\tilde{g}_d(\tau)$.

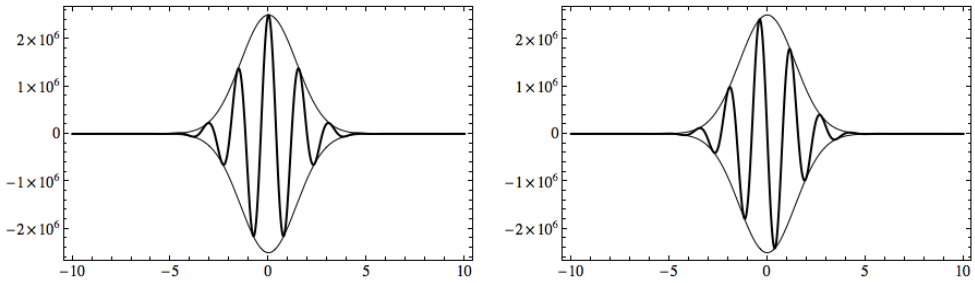

Figure 9. The real part (left) and imaginary part (right) of $\tilde{g}_d(t+\mathrm{i}s)$ with $d=2$ and $s=8$, together with their envelopes.

The 'small' value of $\tilde{g}_d(\tau)$ in the region $s<|t|$ for large $|\tau|$ is therefore the Cauchy kernel. Note that

$$\tilde{g}_d(-\tau)=\frac{1}{2\pi}\int_0^\infty \mathrm{d}\omega\,\mathrm{e}^{\mathrm{i}\omega\tau}\,\mathrm{e}^{-d^2\omega^2/4}=\frac{1}{2\pi}\int_{-\infty}^0 \mathrm{d}\omega\,\mathrm{e}^{-\mathrm{i}\omega\tau}\,\mathrm{e}^{-d^2\omega^2/4} \tag{72}$$

is the analytic continuation of the negative-frequency part $\tilde{g}_d(t)^*$ of $g_d(t)$, as is also clear from (69).

Equation (66) is remarkable. It shows that $\tilde{H}_d(-\mathrm{i}\tau)$ projects out exactly the positive-frequency part of $g_d(\tau)$ by multiplication in the *complex time domain*, precisely as does $H(\omega)$ through (50) in the frequency domain.

Figure 9 shows the real and imaginary parts of $\tilde{g}_d(t+\mathrm{i}s)$ as functions of t with $d=2$ and $s=8$. They are very similar to those of the real and imaginary parts of $g_d(t+\mathrm{i}s)$ (70).

With $g=g_d$, the positive-frequency analytic Huygens relation (53) converges absolutely:

$$\boxed{\frac{\tilde{g}_d(t-r)}{r}=\frac{\alpha^2}{4\pi}\partial_{\alpha'\alpha}\int\frac{\mathrm{d}\hat{\boldsymbol{n}}}{\zeta_r\zeta_e}\tilde{g}_d(t-\zeta).} \tag{73}$$

By (51), the Gaussian wave propagator (59) is given by

$$P_d(x) = \frac{g_d(t-r)}{r} = 2\mathrm{Re}\left\{\frac{\alpha^2}{4\pi}\partial_{\alpha'\alpha}\int\frac{\mathrm{d}\hat{\boldsymbol{n}}}{\zeta_r\zeta_e}\tilde{g}_d(t-\zeta)\right\}. \tag{74}$$

Carrying out the differentiations in (73) gives an expression more suitable for computations:

$$\frac{\tilde{g}_d(t-r)}{r} = \frac{\alpha^2}{4\pi}\int\frac{\mathrm{d}\hat{\boldsymbol{n}}}{\zeta_r\zeta_e}\left[\frac{\zeta_e'}{\zeta_e} - \frac{\zeta_r'}{\zeta_r} + (\zeta_e' - \zeta_r')\partial_t\right]\tilde{g}_d(t-\zeta), \tag{75}$$

where $\zeta_r' = \partial_\alpha\zeta_r$ and $\zeta_e' = \partial_\alpha\zeta_e$, as in (39) after setting $\alpha' = \alpha$. The derivative $\partial_\tau\tilde{g}_d(t-\zeta)$ is easily computed. Since

$$\partial_\tau\tilde{H}_d(-\mathrm{i}\tau) = \frac{1}{\sqrt{\pi}}\partial_\tau\int_{\mathrm{i}\tau/d}^{\infty}\mathrm{d}u\,\mathrm{e}^{-u^2} = \frac{\mathrm{e}^{\tau^2/d^2}}{\mathrm{i}\sqrt{\pi}d} \qquad \text{and} \qquad \partial_\tau g_d(\tau) = -\frac{2\tau}{d^2}g_d(\tau),$$

we have

$$\partial_\tau\tilde{g}_d(\tau) = g_d(\tau)\partial_\tau\tilde{H}_d(-\mathrm{i}\tau) + \tilde{H}_d(-\mathrm{i}\tau)\partial_\tau g_d(\tau) = -\frac{2\tau}{d^2}\left\{\tilde{g}_d(\tau) - \frac{1}{2\pi\mathrm{i}\tau}\right\}. \tag{76}$$

Note that

$$|\tau| \to \infty \qquad \text{with} \qquad |t| > s \quad \Rightarrow \quad \partial_\tau\tilde{g}_d(\tau) = \mathcal{O}(\tau^{-2})$$

because the Cauchy kernel is canceled by (71) and the next term in the asymptotic expansion of $\tilde{g}_d(\tau)$ is $\mathcal{O}(\tau^{-3})$. Inserting this into (75) and using (39) gives an expression without any derivatives, ideal for numerical computations.

We shall now interpret (74) as a representation of P_d by a sum of *pulsed-beam wavelets* radiated by the disks $\mathcal{D}(\alpha\hat{\boldsymbol{n}})$ tangent to the sphere S_R. It suffices to work with the positive-frequency part (73). Recall that

$$x = x_r - x_e = (\boldsymbol{x}_r - \boldsymbol{x}_e, t_r - t_e) = (\boldsymbol{x}, t)$$

represents the spacetime 4-vector from the *emission event* x_e to the *reception event* x_r. Consider the *intermediate complex event* given by[13]

$$z = (\alpha'\hat{\boldsymbol{n}}, \tau), \qquad \text{where} \quad \tau = t_e + \zeta_e \tag{77}$$

is the emission time t_e plus the complex travel time ζ_e from $\boldsymbol{x}_e$ to $\alpha\hat{\boldsymbol{n}}$. Define the *Gaussian pulsed-beam propagator* from z to x_r by

$$\boxed{\tilde{P}_d(x_r - z) = \frac{\tilde{g}_d(t_r - \tau - \zeta_r)}{\zeta_r} = \frac{\tilde{g}_d(t-\zeta)}{\zeta_r}, \qquad t = t_r - t_e, \qquad \zeta = \zeta_r + \zeta_e.} \tag{78}$$

This represents the complex wave amplitude radiated by $\alpha'\hat{\boldsymbol{n}}$ at the complex time τ and received at $\boldsymbol{x}_r$ at time t_r. Thus, (73) reads

$$\tilde{P}_d(x_r - x_e) = \frac{\alpha^2}{4\pi}\partial_{\alpha'\alpha}\int\mathrm{d}\hat{\boldsymbol{n}}\,\tilde{P}_d(x_r - z)\frac{1}{\zeta_e}. \tag{79}$$

The general Gaussianized solution $F_d(x_r)$ in (62) is therefore given by

$$\begin{aligned} F_d(x_r) &= 2\mathrm{Re}\;\tilde{F}_d(x_r), \qquad \text{where} \\ \tilde{F}_d(x_r) &= \frac{\alpha^2}{4\pi}\partial_{\alpha'\alpha}\int\mathrm{d}\hat{\boldsymbol{n}}\int\mathrm{d}x_e\,\tilde{P}_d(x_r - z)\frac{\varrho(x_e)}{\zeta_e}. \end{aligned} \tag{80}$$

The name 'Gaussian pulsed-beam propagator' will be justified in section 6. Pulsed-beam representations of general solutions will be given in section 9.

[13] Recall that $\zeta_e = \zeta_e(\alpha)$ and $\zeta_r = \zeta_r(\alpha')$ and we set $\alpha' = \alpha$ after applying $\partial_{\alpha'\alpha}$.

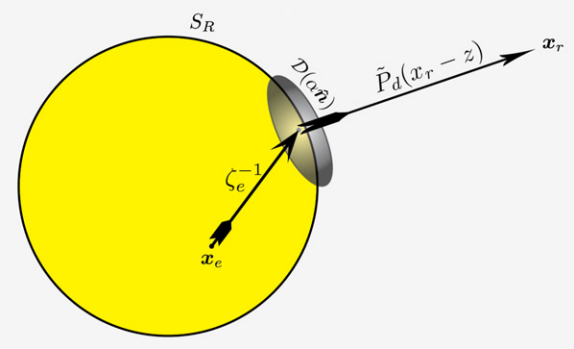

Figure 10. The factor ζ_e^{-1} in (79) represents the reception amplitude at $\alpha\hat{\boldsymbol{n}}$ due to the attenuation suffered in propagating from $\boldsymbol{x}_e$ to $\alpha\hat{\boldsymbol{n}}$, and $\tilde{P}_d(x_r - z)$ represents the propagation of a pulsed beam from the disk $\mathcal{D}(\alpha\hat{\boldsymbol{n}})$ to $\boldsymbol{x}_r$.

6. Pulsed-beam Huygens wavelets

We now show that $\tilde{P}_d(x_r - z)$ is indeed a *pulsed beam* radiated by $\mathcal{D}(\alpha'\hat{\boldsymbol{n}})$ which propagates along $\hat{\boldsymbol{n}}$, with the propagation along $-\hat{\boldsymbol{n}}$ suppressed by $\tilde{g}_d$ as in figure 8. The factor ζ_e^{-1} represents a *complex attenuation* suffered by the spherical wave emitted by the point source at $\boldsymbol{x}_e$ while propagating to $\alpha\hat{\boldsymbol{n}}$. Thus we have a picture, shown in figure 10, of a spherical wave emitted at $\boldsymbol{x}_e$ and *received* at $\alpha\hat{\boldsymbol{n}}$ with 'reception amplitude' ζ_e^{-1}, then re-radiated from $\alpha'\hat{\boldsymbol{n}}$ as a pulsed beam and finally received at $\boldsymbol{x}_r$.[14] The idea of analytically continued fields as reception amplitudes by complex-source disks will be explained in more detail in section 10.

By (78),

$$\tilde{P}_d(x_r - z) = \frac{\tilde{g}_d(t - \zeta)}{\zeta_r} = \frac{\tilde{g}_d(t - \xi + \mathrm{i}\eta)}{\zeta_r}. \tag{81}$$

The properties established for $\tilde{g}_d$ show that the magnitude of $\tilde{P}_d(x_r - z)$ is an increasing function of η that attains its greatest values in the frontal zone S_R^+ nearest to $\boldsymbol{x}_r$; see figure 5. Some insight can be gained by noting that

$$g_d(t - \zeta) = g_d(t - \xi)\, \mathrm{e}^{\eta^2/d^2}\, \mathrm{e}^{-2\mathrm{i}\eta(t-\xi)/d^2}$$

and expanding

$$\tilde{P}_d(x_r - z) = \zeta_r^{-1} \tilde{H}_d(\eta - \mathrm{i}(t - \xi))\, \mathrm{e}^{\eta^2/d^2} g_d(t - \xi)\, \mathrm{e}^{-2\mathrm{i}\eta(t-\xi)/d^2}. \tag{82}$$

- At a given time t, the factor $g_d(t - \xi)$ ensures that $\tilde{P}_d(x_r - z)$ is concentrated on a shell of thickness $\sim 2d$ around the surface $\xi = t$. $\tilde{P}_d$ has significant values only when t is in the range of ξ, which varies with $\hat{\boldsymbol{n}} \in S^2$ over a positive interval containing the *line of sight* time $r = |\boldsymbol{x}_r - \boldsymbol{x}_e|$, the minimum time required to travel from $\boldsymbol{x}_e$ to $\boldsymbol{x}_r$ at speed $c = 1$. If instead we vary $x_r = (\boldsymbol{x}_r, t_r)$ but fix x_e and $\hat{\boldsymbol{n}}$, this means that the oblate spheroid given by

  $$\mathcal{O}_{\xi_r} = \mathcal{O}_{t-\xi_e}$$

  is a *wavefront* of $\tilde{P}_d(x_r - z)$ expanding with $t = t_r - t_e$. This gives a direct meaning to ξ_r: *it is a variable whose level surfaces are wavefronts.*

[14] We are ignoring the derivatives $\partial_{\alpha'\alpha}$, so this interpretation is somewhat schematic.

- From the behavior of $\tilde{g}_d$, it follows that the factor $\tilde{H}_d(\eta - \mathrm{i}(t-\xi))\,\mathrm{e}^{\eta^2/d^2}$ in (82) is an increasing function of η that boosts the incoming wave when $\eta > 0$ while suppressing it when $\eta < 0$.
- Due to the factor $\mathrm{e}^{-2\mathrm{i}\eta(t-\xi)/d^2}$, $\tilde{P}_d(x_r - z)$ oscillates at the compression frequency

$$\omega_d(\eta) = \frac{2\eta}{d^2}, \tag{83}$$

which depends on $\boldsymbol{x}_r$ for a given $\hat{\boldsymbol{n}}$ and on $\hat{\boldsymbol{n}}$ for a given $\boldsymbol{x}_r$. This is perturbed slightly by the phase of $\tilde{H}_d(\eta - \mathrm{i}(t-\xi))$.

By interpreting every factor in (82), we have thus understood $\tilde{P}_d(x_r - z)$ as a *pulsed beam with wavefronts* $\mathcal{O}_{\xi_r}$ *propagating along the semi-hyperboloid* $\mathcal{H}_{\eta_r}$ at the compression frequency ω_d.

Consider the limit of (79) as $a, a' \to 0$:

$$\tilde{P}_d(x_r - x_e) = \frac{R^2}{4\pi}\partial_{R'R}\int \mathrm{d}\hat{\boldsymbol{n}}\,\tilde{P}_d(x_r - x)\frac{1}{r_e},$$

where $x = (R'\hat{\boldsymbol{n}}, t_e + r_e)$ is a reception event on $S_{R'}$ at the arrival time $t_e + r_e$ of a spherical wave radiated from $\boldsymbol{x}_e$ at t_e. As a function of x_r, $\tilde{P}_d(x_r - x)$ is the positive-frequency part of a real Huygens wavelet emitted from x.[15] By complexifying the sphere, we have deformed the original *spherical* Huygens wavelets to pulsed beams (78):

$$\tilde{P}_d(x_r - x) \to \tilde{P}_d(x_r - z).$$

This deformation acts on space so that spheres become oblate spheroids and cones become semi-hyperboloids, as in (16). In the process of being deformed, the spherical Huygens wavelets are *compressed* in the forward direction and *stretched* in the backward direction[16]. Being complex, the compression introduces a phase which gives a measure of its strength. This is why we call ω_d the 'compression frequency.' As expected,

$$a, a' \to 0 \;\Rightarrow\; \eta \to 0 \;\Rightarrow\; \omega_d \to 0.$$

The *time-domain radiation pattern* of a radiation field $F(\boldsymbol{x}, t)$ with cylindrical symmetry is, by definition [HY99], the function $\mathcal{F}(\theta, t)$ satisfying the far-field relation

$$F(\boldsymbol{x}, t) \sim \frac{\mathcal{F}(\theta, t - r)}{r}.$$

To compute the radiation pattern of $\tilde{P}_d(x_r - z)$ *relative to the coordinate system of the disk* $\mathcal{D}(\alpha'\hat{\boldsymbol{n}})$, assume the observer is far from the disk[17]. Taking $\alpha' = \alpha$ for simplicity, (23) gives

$$r_r \gg a \;\Rightarrow\; \xi_r \sim r_r, \qquad \eta_r \sim a\hat{\boldsymbol{r}}_r \cdot \hat{\boldsymbol{n}} \equiv a\cos\theta_r,$$

so that

$$\xi \sim r_r + \xi_e, \qquad \eta \sim a\cos\theta_r - \eta_e.$$

[15] Although $P_d(x_r - x) = 2\,\mathrm{Re}\,\tilde{P}_d(x_r - x)$ is not a *wave* because $g_d(t - r)$ does not oscillate, applying the derivative $\partial_{\alpha'\alpha}$ gives it some oscillation. For example,

$$\partial_\alpha g_d(t-\zeta) = -\zeta_e'\partial_t g_d(t-\zeta) = \frac{2\zeta_e'}{d^2}(t-\zeta)g_d(t-\zeta)$$

is a one-cycle wave.

[16] In a certain sense, they are *Doppler scaled* positively in the forward direction and negatively in the backward direction [K94].

[17] Since we are keeping $\hat{\boldsymbol{n}}$ fixed but varying $\boldsymbol{x}_r$, it is unnecessary to assume that $r_r \gg R$. Only the relative vector $\boldsymbol{r}_r = \boldsymbol{x}_r - R\hat{\boldsymbol{n}}$ enters the above discussion.

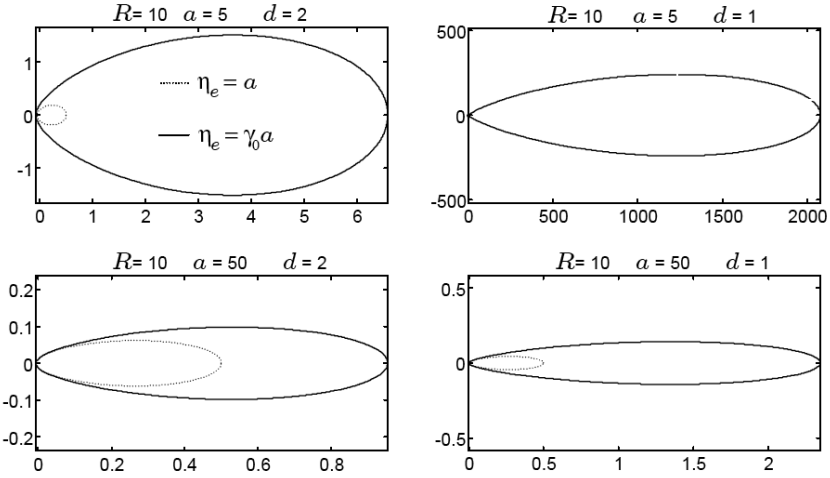

Figure 11. Peak-time radiation patterns of $\tilde{P}_d(x_r - z)$ for $d = 1, 2$ and $a = 5, 50$. In each case, we have plotted the beams with the *weakest* pattern ($\eta_e = a$) and the *strongest* pattern ($\eta_e = \gamma_0 a$). For $a = 5$ and $d = 1$, the weakest pattern is so weak that it cannot be seen.

The factor ζ_r^{-1} in (78) can be approximated by r_r^{-1} since $r_r \gg a$ and $\xi_e \leqslant r_e < 2a$. Thus,

$$\tilde{P}_d(x_r - z) \sim \frac{\tilde{g}_d(t' - r_r + \mathrm{i}(a\cos\theta_r - \eta_e))}{r_r}, \qquad \text{where} \quad t' = t - \xi_e.$$

Hence the radiation pattern of $\tilde{P}_d(x_r - z)$ is

$$\mathcal{F}(\theta_r, t) = \tilde{g}_d(t' + \mathrm{i}(a\cos\theta_r - \eta_e)). \tag{84}$$

The *peak radiation time* is $t' = 0$, when $t = \xi_e$ is the arrival time at $\mathcal{D}(\alpha\hat{\boldsymbol{n}})$ of the emitted wave. Figure 11 shows polar plots of the peak-time radiation patterns for two values of a in the two extreme cases with

$$\eta_e = \gamma_0 a \qquad \text{and} \qquad \eta_e = a,$$

where

$$\gamma_0 = \lim_{|\boldsymbol{x}_e| \to R} \gamma = \sqrt{1 - \frac{R^2}{R^2 + a^2}} = \frac{a}{\sqrt{R^2 + a^2}} < 1$$

as in (20). This lower bound applies to *every source supported in* S_R.

Since $|\tilde{g}_d(t + \mathrm{i}s)|$ is an increasing function of s, the upper bound $\eta_e = a$ is expected to produce a weaker pattern than the lower bound $\eta_e = \gamma_0 a$, as already discussed beneath (48). This is borne out in figure 11, where the pattern with $\eta_e = a$ for $a = 5$ and $d = 1$ is so weak that it is invisible. On the other hand for $a = 50$, the disk is so large as to dwarf the sphere. Since $\gamma_0 \approx 0.98$ in this case, there is not a great difference between the lower and upper bounds of η_e. This is the reason why both patterns are visible in the lower figures, and why both are much weaker than the patterns with $a = 5$ and $\eta_e = \gamma_0 a$.

We have thus established (79) as a *pulsed-beam representation* of $\tilde{P}_d(x_r - x_e)$. Since the pulsed beams $\tilde{P}_d(x_r - z)$ are deformations of Huygens' spherical wavelets, it is reasonable to call them *pulsed-beam Huygens wavelets.* By taking the real part and convolving with a general source ϱ, as in (62), we obtain a pulsed-beam representation of the Gaussianized version $F_d(x)$ of any radiation field $F(x)$.

7. Some remarks

(1) The radiation patterns of extended sources generally have *sidelobes*, which are interference patterns between parts of the wave arriving from different parts of the source. Sidelobes of beams often stray widely from the intended direction of propagation, causing problems in applications such as communications, remote sensing and radar [S98]. However, note that the radiation pattern (84) is *real* at the peak time $t' = 0$ and it decays monotonically with increasing θ_r, as confirmed by figure 11. It therefore has no sidelobes, and that makes it potentially very useful. If we include the time-dependence around $t' = 0$, the radiation pattern acquires a phase factor $\mathrm{e}^{-\mathrm{i}\omega_d t'}$ and $2\,\mathrm{Re}\,\mathcal{F}(\theta_r, t)$, the radiation pattern of $P_d(x_r - z)$, acquires sidelobes. But these are confined to the narrow *envelope* of $2|\mathcal{F}(\theta_r, t)|$ and do not cause the usual problems.

(2) To fully justify the name 'pulsed-beam propagator', consider $\tilde{P}_d(x_r - z)$ as a function of x_r with z fixed. It is singular on the branch cut $\mathcal{D}(\alpha'\hat{\boldsymbol{n}})$ of $\zeta_r(\alpha')$ and analytic elsewhere, hence

$$\boldsymbol{x}_r \notin \mathcal{D}(\alpha'\hat{\boldsymbol{n}}) \;\Rightarrow\; \Box_r \tilde{P}_d(x_r - z) = 0,$$

where $\Box_r$ is the wave operator with respect to x_r. $\tilde{P}_d(x_r - z)$ is therefore the wave radiated by the disk $\mathcal{D}(\alpha'\hat{\boldsymbol{n}})$. The precise source of $\tilde{P}_d(x_r - z)$ is a generalized function $\tilde{\delta}_d(x_r - z)$ supported on $\boldsymbol{x}_r \in \mathcal{D}(\alpha'\hat{\boldsymbol{n}})$; see equation (107) in section 10.

(3) Taking the complex conjugate of (73) and substituting $\alpha, \alpha' \to \alpha^*, \alpha'^*$ (which is permitted since the left side is independent of α and α' and the domain (32) is symmetric under conjugation) gives the negative-frequency component in the form

$$\frac{\tilde{g}_d(t - r)^*}{r} = \frac{\alpha^2}{4\pi}\partial_{\alpha'\alpha} \int \frac{\mathrm{d}\hat{\boldsymbol{n}}}{\zeta_r \zeta_e} \tilde{g}_d(t - \zeta^*)^*, \tag{85}$$

where we have used the reality conditions (18)

$$\zeta_e(\alpha^*)^* = \zeta_e(\alpha), \qquad \zeta_r(\alpha'^*)^* = \zeta_r(\alpha').$$

Thus, $\tilde{g}_d(\tau)$ satisfies the reality condition

$$\tilde{g}_d(\tau^*)^* = \tilde{g}_d(\tau),$$

which also follows directly from (64). Adding (73) and (85) gives an *alternative* form of the analytic Huygens relation[18]

$$\frac{g_d(t - r)}{r} = \frac{\alpha^2}{4\pi}\partial_{\alpha'\alpha} \int \frac{\mathrm{d}\hat{\boldsymbol{n}}}{\zeta_r \zeta_e} g_d(t - \zeta), \tag{86}$$

which is simpler than (74) as it does not split up the positive and negative frequencies. However, we find that while (86) is numerically valid, it does *not* lead to a compressed representation of radiation fields. The problem is the substitutions $\alpha \to \alpha^*, \alpha' \to \alpha'^*$. For $\alpha = R + \mathrm{i}a$ with $a > 0$,

$$\alpha^*\hat{\boldsymbol{n}} = R\hat{\boldsymbol{n}} - \mathrm{i}a\hat{\boldsymbol{n}}. \tag{87}$$

Hence the disk $\mathcal{D}(\alpha^*)$, while still tangent to $R\hat{\boldsymbol{n}}$, radiates a pulsed beam along $-\hat{\boldsymbol{n}}$, i.e. to the *interior* of the sphere. Eventually, this beam leaves the sphere and continues to propagate, weakened, in the direction of $-\hat{\boldsymbol{n}}$, but this is clearly an inefficient way to represent radiation. Although (86) is *mathematically* correct in the sense that the integral on the right converges absolutely to $\tilde{P}_d(x_r - x_e)$, this inefficiency shows up in

[18] Equation (87) can also be obtained directly from (49) with $\hat{g}_d(\omega) = \mathrm{e}^{-d^2\omega^2/4}$.

the appearance of very large numbers which spoil the compression and easily overwhelm computational software, thus introducing huge errors; see the discussion at the end of section 11.

(4) In view of the previous remark, we can say that the positive-frequency part of (49) is 'good' while its negative-frequency part is 'bad'. The situation would be reversed for the *interior problem*, where a source is given outside of S_R and we seek to represent the field inside S_R as a superposition of pulsed beams. The pulsed-beam analysis and synthesis of interior fields is very similar to that of exterior fields and will be treated elsewhere.

(5) The pulsed-beam representation (80) of general radiation fields suggests an important application: given a receiver at $\boldsymbol{x}_r$, the most significant contributions are expected to come from disks radiating approximately in the direction of $\boldsymbol{x}_r$, whose centers $R\hat{\boldsymbol{n}}$ are in the frontal zone S_R^+. That is, by using only the 'relevant' wavelets propagating toward a given observer, we obtain a *compressed* representation of $F_d(x_r)$. This is illustrated by a numerical example in section 11.

8. Huygens reproducing relation for pulsed beams

The time-domain version (79) of the analytic Huygens principle treats emission and reception asymmetrically: propagation from x_e to z is represented by ζ_e^{-1}, whereas propagation from z to x_r is represented by $\tilde{P}_d(x_r - z)$. In this section, we construct a more complete picture of this process which has a detailed and appealing physical interpretation. For this we shall need to Gaussianize both the emission time t_e and the reception time t_r. Thus let d_e and d_r be Gaussian duration parameters for t_e and t_r and let

$$d = \sqrt{d_e^2 + d_r^2},$$

which is the duration parameter for the entire transmission process. Let

$$z_\alpha = (\alpha\hat{\boldsymbol{n}}, \tau), \qquad z_{\alpha'} = (\alpha'\hat{\boldsymbol{n}}, \tau), \qquad \text{where} \quad \tau = t + \mathrm{i}s \tag{88}$$

is a free complex time variable. When $\tau = t_e + \zeta_e$, i.e. $t = t_e + \xi_e$ and $s = \eta_e$, (88) reduces to (77). The propagations from x_e to z_α and $z_{\alpha'}$ to x_r are governed by

$$\tilde{P}_{d_e}(z_\alpha - x_e) = \frac{\tilde{g}_{d_e}(\tau - t_e - \zeta_e)}{\zeta_e}$$
$$\tilde{P}_{d_r}(x_r - z_{\alpha'}) = \frac{\tilde{g}_{d_r}(t_r - \tau - \zeta_r)}{\zeta_r}$$

with

$$\tilde{g}_{d_e}(\tau - t_e - \zeta_e) = \frac{1}{2\pi}\int_0^\infty \mathrm{d}\omega\, \mathrm{e}^{-\mathrm{i}\omega(t - t_e - \zeta_e + \mathrm{i}s)}\, \mathrm{e}^{-d_e^2\omega^2/4}$$
$$\tilde{g}_{d_r}(t_r - \tau - \zeta_r) = \frac{1}{2\pi}\int_0^\infty \mathrm{d}\omega\, \mathrm{e}^{-\mathrm{i}\omega(t_r - t - \zeta_r - \mathrm{i}s)}\, \mathrm{e}^{-d_r^2\omega^2/4}.$$

Applying the Fourier transform in $t' = t - t_e$ to the first equation and in $t'' = t_r - t$ to the second equation gives

$$\begin{aligned}
&\int_{-\infty}^\infty \mathrm{d}t'\, \mathrm{e}^{\mathrm{i}\omega t'}\, \tilde{g}_{d_e}(t' - \zeta_e + \mathrm{i}s) = H(\omega)\, \mathrm{e}^{\mathrm{i}\omega(\zeta_e - \mathrm{i}s)}\, \mathrm{e}^{-d_e^2\omega^2/4} \\
&\int_{-\infty}^\infty \mathrm{d}t''\, \mathrm{e}^{\mathrm{i}\omega t''}\, \tilde{g}_{d_r}(t'' - \zeta_r - \mathrm{i}s) = H(\omega)\, \mathrm{e}^{\mathrm{i}\omega(\zeta_r + \mathrm{i}s)}\, \mathrm{e}^{-d_r^2\omega^2/4}.
\end{aligned} \tag{89}$$

Multiplying (37) by $H(\omega)\,\mathrm{e}^{-d^2\omega^2/4} = H(\omega)^2\,\mathrm{e}^{-d^2\omega^2/4}$ gives

$$H(\omega)\frac{\mathrm{e}^{\mathrm{i}\omega r}}{r}\mathrm{e}^{-d^2\omega^2/4} = \frac{\alpha^2}{4\pi}\partial_{\alpha'\alpha}\int \mathrm{d}\hat{\boldsymbol{n}}\left[H(\omega)\frac{\mathrm{e}^{\mathrm{i}\omega\zeta_r}\,\mathrm{e}^{-d_r^2\omega^2/4}}{\zeta_r}\right]\left[H(\omega)\frac{\mathrm{e}^{\mathrm{i}\omega\zeta_e}\,\mathrm{e}^{-d_e^2\omega^2/4}}{\zeta_e}\right]$$
$$= \frac{\alpha^2}{4\pi}\partial_{\alpha'\alpha}\int \mathrm{d}\hat{\boldsymbol{n}}\left[H(\omega)\frac{\mathrm{e}^{\mathrm{i}\omega(\zeta_r+\mathrm{i}s)}\,\mathrm{e}^{-d_r^2\omega^2/4}}{\zeta_r}\right]\left[H(\omega)\frac{\mathrm{e}^{\mathrm{i}\omega(\zeta_e-\mathrm{i}s)}\,\mathrm{e}^{-d_e^2\omega^2/4}}{\zeta_e}\right].$$

Taking the inverse Fourier transform and writing the time variable as $t_r - t_e$ gives

$$\frac{\tilde{g}_d(t_r - t_e - r)}{r} = \frac{\alpha^2}{4\pi}\partial_{\alpha'\alpha}\int \mathrm{d}\hat{\boldsymbol{n}}\int_{-\infty}^{\infty}\mathrm{d}t\,\frac{\tilde{g}_{d_r}(t_r - \tau - \zeta_r)}{\zeta_r}\,\frac{\tilde{g}_{d_e}(\tau - t_e - \zeta_e)}{\zeta_e}.$$

We have thus proved the following result.

Theorem 2. *The Gaussian pulsed-beam propagator $\tilde{P}_d$ satisfies the following complex spacetime Huygens reproducing relation:*

$$\boxed{\tilde{P}_d(x_r - x_e) = \frac{\alpha^2}{4\pi}\partial_{\alpha'\alpha}\int \mathrm{d}\hat{\boldsymbol{n}}\int_{-\infty}^{\infty}\mathrm{d}t\,\tilde{P}_{d_r}(x_r - z_{\alpha'})\tilde{P}_{d_e}(z_\alpha - x_e).} \tag{90}$$

Remark 1. The complex spacetime 4-vector $z_\alpha = (\alpha\hat{\boldsymbol{n}}, t + \mathrm{i}s)$ represents a *pulsed receiving disk* with a 'Gaussian' reception interval $[t - d_e, t + d_e]$, which we denote by[19]

$$\mathcal{D}_{d_e}(z_\alpha) \equiv \mathcal{D}(\alpha\hat{\boldsymbol{n}}) \times I_{d_e}(t) \subset \mathbb{R}^4, \qquad \text{where} \quad I_{d_e}(t) = [t - d_e, t + d_e]. \tag{91}$$

Just as $\alpha\hat{\boldsymbol{n}} \in \mathbb{C}^3$ represents the extended object $\mathcal{D}(\alpha\hat{\boldsymbol{n}})$ in space, so does $z \in \mathbb{C}^4$ represent the extended object $\mathcal{D}_{d_e}(z)$ in spacetime. Similarly, $z_{\alpha'}$ represents a *pulsed emitting disk*

$$\mathcal{D}_{d_r}(z_{\alpha'}) \equiv \mathcal{D}(\alpha'\hat{\boldsymbol{n}}) \times I_{d_r}(t). \tag{92}$$

The relation between pulsed-beam emitters and receivers will be explained in greater detail in section 10.

Remark 2. Equation (90) has a simple interpretation which, unlike (79), treats emission and reception symmetrically. It states that the spherical wave emitted from the point source x_e is received by $\mathcal{D}_{d_e}(z_\alpha)$, then immediately re-emitted by $\mathcal{D}_{d_r}(z_{\alpha'})$, and finally received at x_r. The direct propagator $\tilde{P}_d(x_r - x_e)$ is recovered by integrating over all directions $\hat{\boldsymbol{n}}$ and intermediate times t and then applying $(\alpha^2/4\pi)\partial_{\alpha'\alpha}$.

Remark 3. The integral over t can be viewed as a *contour integral* in τ, with the left side independent of s due to analyticity. In fact, s is allowed to depend on $\hat{\boldsymbol{n}}$ (and even on t). For a general emission source $\varrho_e(x_e)$ and receiving source $\varrho_r(x_r)$, where there are additional integrations over x_e and x_r, s may also be allowed to depend on x_e and x_r.

Remark 4. The formal symmetry of (90) with respect to emission and reception is of more than purely academic interest. To formulate pulsed-beam representations for the *interior field* given an exterior source ϱ, we must reverse the roles of x_e and x_r and use the *advanced* wave propagator:

$$P(x) \to P'(x) = \frac{\delta(t + r)}{r}. \tag{93}$$

Then (90) transforms to a pulsed-beam representation of the interior field but (79) fails to do so. However, to get an *efficient* representation, we must also replace α, α' by their complex

[19] The role of $s = \mathrm{Im}\,\tau$ will be explained below.

conjugates, as discussed beneath (87), since we now want the pulsed beams to propagate *inward*.

The properties of $\tilde{g}_d$ place some practical constraints on s. Let

$$\begin{aligned}\tau_e &= \tau - t_e - \zeta_e = t - t_e - \xi_e + \mathrm{i}(s - \eta_e)\\ \tau_r &= t_r - \tau - \zeta_r = t_r - t - \xi_r + \mathrm{i}(\eta_r - s),\end{aligned} \tag{94}$$

so that

$$\tilde{P}_{d_e}(z_\alpha - x_e) = \frac{\tilde{g}_{d_e}(\tau_e)}{\zeta_e} \qquad \text{and} \qquad \tilde{P}_{d_r}(x_r - z_{\alpha'}) = \frac{\tilde{g}_{d_r}(\tau_r)}{\zeta_r}. \tag{95}$$

The compression frequencies of the interior and exterior pulsed beams, defined as in (83), are

$$\omega_e = \frac{2(s - \eta_e)}{d_e^2}, \qquad \omega_r = \frac{2(\eta_r - s)}{d_r^2}, \tag{96}$$

and the propagators in (90) will be very small unless

$$\omega_e > 0, \qquad \omega_r > 0, \tag{97}$$

respectively. If *both* inequalities hold, they imply

$$\eta_e < s < \eta_r, \tag{98}$$

which is consistent with $\eta = \eta_r - \eta_e > 0$. For example,

$$s = \frac{\eta_r + \eta_e}{2} \;\Rightarrow\; \omega_e = \frac{\eta}{d_e^2} \qquad \text{and} \qquad \omega_r = \frac{\eta}{d_r^2}. \tag{99}$$

Since $\eta_r > \eta_e$ for the dominant beams, the condition (97) is indeed satisfied by (99), showing that (98) is sufficient as well as necessary. Although our proof of (90) is theoretically valid for all choices of s, the computation can be expected to be *inefficient* for values of s violating (97). For example, if s is large and positive, then $\tilde{P}_{d_e}(z_\alpha - x_e)$ is very large and $\tilde{P}_{d_r}(x_r - z_{\alpha'})$ is very small. Conversely, choosing s large and negative makes $\tilde{P}_{d_e}$ very small and $\tilde{P}_{d_r}$ very large. Such choices introduce unnecessary *noise* into the computation, thus reducing its efficiency and even causing errors when the machine capacity is exceeded, which does in fact occur rapidly due to the exponential growth. Note that choosing s in the 'good' interval (98) makes it dependent on $\hat{\boldsymbol{n}}$, which is permissible as explained above.

Numerical calculations confirm that all values of s in the interval $[\eta_e, \eta_r]$ give stable results and that instabilities build up rapidly when s strays outside this interval.

9. Analytic Huygens relation for general solutions

Let $\varrho(x) = \varrho(\boldsymbol{x}, t)$ be a time-dependent source distribution bounded in space, and choose R so that $\varrho(\boldsymbol{x}, t)$ is supported in the open ball $|\boldsymbol{x}| < R$ at all times[20]. The radiated field F is given by

$$F(x) = \int \mathrm{d}x_e\, P(x - x_e)\varrho(x_e), \tag{100}$$

where P is the retarded wave propagator (54). Now Gaussianize the emission time t_e by

$$\varrho_{d_e}(\boldsymbol{x}_e, t_e) = \int_{-\infty}^{\infty} \mathrm{d}t'_e\, g_{d_e}(t_e - t'_e)\varrho(\boldsymbol{x}_e, t'_e), \qquad d_e > 0.$$

[20] This is always possible if ϱ is compactly supported in time as well as space. If ϱ is spatially bounded at all times but does not remain in a bounded spatial region (for example, if it drifts at some velocity $\boldsymbol{v} \neq \boldsymbol{0}$), then a generalization of (90) based on a spacetime version of Green's second identity must be used.

Then the wave arriving at x is (by the associativity of convolutions)

$$F_{d_e}(x) = \int \mathrm{d}x_e\, P(x - x_e)\varrho_{d_e}(x_e) = \int \mathrm{d}x_e\, P_{d_e}(x - x_e)\varrho(x_e), \tag{101}$$

where P_{d_e} is the Gaussian propagator (59). The spatial integral is over the support of ϱ in the interior of the sphere S_R. Both sides of (101) can be continued analytically to the complex spacetime points

$$x \to z_\alpha = (\alpha\hat{\boldsymbol{n}}, t + \mathrm{i}s),$$

since the integration over $\boldsymbol{x}_e$ does not encounter any of the branch cuts of $\zeta_e = \sqrt{(\alpha\hat{\boldsymbol{n}} - \boldsymbol{x}_e)^2}$. The analytic continuation of the positive-frequency part $\tilde{F}_{d_e}(x)$ of (101) is

$$\tilde{F}_{d_e}(z_\alpha) = \int \mathrm{d}x_e\, \tilde{P}_{d_e}(z_\alpha - x_e)\varrho(x_e). \tag{102}$$

Convolving (90) with ϱ gives

$$\boxed{\tilde{F}_d(x_r) = \frac{\alpha^2}{4\pi}\partial_{\alpha'\alpha}\int \mathrm{d}\hat{\boldsymbol{n}} \int \mathrm{d}t\, \tilde{P}_{d_r}(x_r - z_{\alpha'})\tilde{F}_{d_e}(z_\alpha),} \tag{103}$$

where the reception time t_r has also been Gaussianized by convolving with $\tilde{g}_{d_r}$, so that the total duration parameter is $d = \sqrt{d_e^2 + d_r^2}$.

The analytic Huygens relation (90) for propagators thus implies a pulsed-beam representation for arbitrary solutions with spatially bounded sources. As shown in section 10, the coefficient $\tilde{F}_{d_e}(z_\alpha)$ in this superposition is the *reception amplitude* of the interior field F_{d_e} by the pulsed disk $\mathcal{D}_{d_e}(z_\alpha)$.

10. Pulsed-beam reception and emission

The purpose of this section is to justify the interpretation of $\tilde{F}_{d_e}(z_\alpha)$ in (103) as the *reception amplitude* of the field F by the pulsed disk $\mathcal{D}_{d_e}(z_\alpha)$ defined in (91). By the wave equation

$$\Box F(x) = 4\pi\varrho(x),$$

(102) can be written as a relation between $\tilde{F}_{d_e}(z_\alpha)$ and $F(x_e)$,

$$\tilde{F}_{d_e}(z_\alpha) = \frac{1}{4\pi}\int \mathrm{d}x_e\, \tilde{P}_{d_e}(z_\alpha - x_e)\,\Box_e F(x_e), \tag{104}$$

where $\Box_e$ is the wave operator in x_e and

$$z_\alpha = (\alpha\hat{\boldsymbol{n}}, \tau) = x + \mathrm{i}y, \qquad x = (R\hat{\boldsymbol{n}}, t), \qquad y = (a\hat{\boldsymbol{n}}, s).$$

Integrating by parts twice gives[21]

$$\tilde{F}_{d_e}(z_\alpha) = \frac{1}{4\pi}\int \mathrm{d}x_e\, \Box_e \tilde{P}_{d_e}(z_\alpha - x_e)F(x_e). \tag{105}$$

To make sense of this, note that in *real* spacetime ($y \to 0$) we have (61)

$$\Box_e P_{d_e}(x - x_e) = 4\pi g_{d_e}(t - t_e)\delta(\boldsymbol{x} - \boldsymbol{x}_e) \equiv 4\pi\delta_{d_e}(x - x_e), \tag{106}$$

whose positive-frequency part is

$$\Box_e \tilde{P}_{d_e}(x - x_e) = 4\pi\tilde{g}_{d_e}(t - t_e)\delta(\boldsymbol{x} - \boldsymbol{x}_e) \equiv 4\pi\tilde{\delta}_{d_e}(x - x_e). \tag{107}$$

[21] $\tilde{P}_{d_e}(z_\alpha - x_e)$ is singular when $\boldsymbol{x}_e \in \mathcal{D}(\alpha\hat{\boldsymbol{n}})$, so the right-hand side of (105) must be treated carefully. The wave operator $\Box_e$ acts on $\tilde{P}_{d_e}(z_\alpha - x_e)$ in a *distributional* sense, just as it acts on $P_{d_e}(x - x_e)$ to give $4\pi\delta_{d_e}(x - x_e)$. The resulting distribution $\tilde{\delta}_{d_e}$ can be computed rigorously using the methods developed in [K0, K3, K4, K5, D8] and will be studied in detail elsewhere. Here we explain the main ideas in an intuitive and informal way.

We now *define* the source distribution $\tilde{\delta}_{d_e}(z_\alpha - x_e)$ of $\tilde{P}_{d_e}(z_\alpha - x_e)$ by extending this to complex spacetime:

$$4\pi\tilde{\delta}_{d_e}(z_\alpha - x_e) \equiv \Box_e \tilde{P}_{d_e}(z_\alpha - x_e). \tag{108}$$

Since $\tilde{P}_{d_e}(z_\alpha - x_e)$ is analytic whenever $\boldsymbol{x}_e \notin \mathcal{D}(\alpha\hat{\boldsymbol{n}})$, it follows from (106) that $\Box_e \tilde{P}_{d_e}(z_\alpha - x_e) = 0$ at such $\boldsymbol{x}_e$. Hence, the distribution $\tilde{\delta}_{d_e}(z_\alpha - x_e)$ is supported in $\boldsymbol{x}_e \in \mathcal{D}(\alpha\hat{\boldsymbol{n}})$ at all times. It is also localized in a 'Gaussian' sense in time around the interval $I_{d_e}(t)$; thus, it is effectively localized in the pulsed disk $x_e \in \mathcal{D}_{d_e}(z_\alpha)$.

In other words, the wave operator $\Box_e$ ignores all the *analytic* behavior of $\tilde{P}_{d_e}(z_\alpha - x_e)$ and nails down its *singular* behavior, consisting of a discontinuity across the branch cut $\mathcal{D}(\alpha\hat{\boldsymbol{n}})$ and infinity along the branch circle $\partial\mathcal{D}(\alpha\hat{\boldsymbol{n}})$. All this is possible only in the distributional sense. Combining (105) and (108) gives

$$\boxed{\tilde{F}_{d_e}(z_\alpha) = \int \mathrm{d}x_e \tilde{\delta}_{d_e}(z_\alpha - x_e) F(x_e),} \tag{109}$$

which is the *analytic deformation* of F. Equation (109) shows that $\tilde{F}_{d_e}(z_\alpha)$ is the reception amplitude of $F(x_e)$ by the receiving source $\tilde{\delta}_{d_e}(z_\alpha - x_e)$, confirming our claim.

Remark 1. The distribution $\tilde{\delta}_{d_e}$ includes a *dipole layer*, represented by a first-order differential operator acting on $F(x_e)$ [K0, K3]. Consequently, the right-hand side of (109) contains the values of both F and its partial derivatives.

11. Compressed representations of radiation fields

We now demonstrate that the computational properties of the Huygens representation depend strongly on the disk radius a and there can be a significant advantage to choosing a complex sphere over a real sphere in numerical calculations.

Throughout this section, the source is at $\boldsymbol{x}_e = (0, 0, 2.5)$ and has Gaussian time dependence $g_d(t)$ with $d = 0.3\sqrt{2}$. The reception point is in the far zone on the positive x-axis. We consider three spheres with $R = 10$ and disk radii $a = 0, 5, 50$. For $a = 0$, the sphere is real and the pulsed-beam representation reduces to the classical Huygens representation.

Let

$$\mathcal{I}_d^\alpha(\hat{\boldsymbol{n}}, t) = 2\mathrm{Re}\left\{\frac{\alpha^2}{4\pi\zeta_r\zeta_e}\left[\frac{\zeta_e'}{\zeta_e} - \frac{\zeta_r'}{\zeta_r} + (\zeta_e' - \zeta_r')\partial_t\right]\tilde{g}_d(t-\zeta)\right\}, \qquad \zeta = \zeta_r + \zeta_e, \tag{110}$$

where the dependence on $\boldsymbol{x}_e$ and $\boldsymbol{x}_r$ is implicit and $\partial_t\tilde{g}_d(t-\zeta)$ is given by (76). Then (75) reads

$$P_d(\boldsymbol{x}, t) = 2\mathrm{Re}\ \tilde{P}_d(\boldsymbol{x}, t) = \int \mathrm{d}\hat{\boldsymbol{n}}\mathcal{I}_d^\alpha(\hat{\boldsymbol{n}}, t), \qquad (\boldsymbol{x}, t) = x_r - x_e, \qquad r = |\boldsymbol{x}|. \tag{111}$$

Figure 12 shows $\mathcal{I}_d^\alpha$ evaluated at the peak time $t = r$, where $P_d(\boldsymbol{x}, t)$ attains its maximum value $g_d(0)/r$. The top plot shows that $\mathcal{I}_d^\alpha$ for the real sphere is significantly nonzero only on a ring centered on the *line of sight* point from $\boldsymbol{x}_e$ to $\boldsymbol{x}_r$. We can explain this behavior as follows: for $a = 0$,

$$\zeta_e = |R\hat{\boldsymbol{n}} - \boldsymbol{x}_e| \equiv r_e \qquad \text{and} \qquad \zeta_r = |\boldsymbol{x}_r - R\hat{\boldsymbol{n}}| \equiv r_r$$

satisfy the triangle inequality

$$r_r + r_e \geqslant r \equiv |\boldsymbol{x}_r - \boldsymbol{x}_e|,$$

with equality if and only if $R\hat{\boldsymbol{n}}$ is the line-of-sight point. Now

$$\tilde{g}_d(r - \zeta) = \tilde{H}_d(-\mathrm{i}(r - r_r - r_e))g_d(r - r_r - r_e)$$

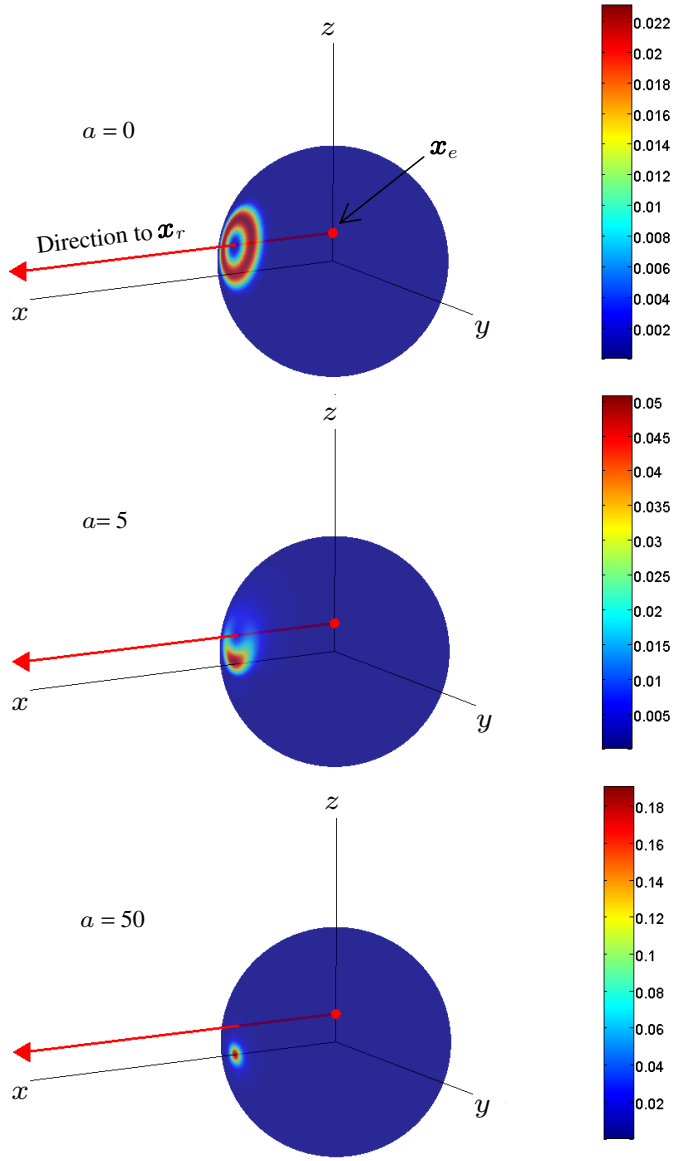

Figure 12. Magnitudes of $\mathcal{I}_d^\alpha$ with $R = 10$ at the peak time $t = r$ and $a = 0$ (top), $a = 5$ (middle) and $a = 50$ (bottom). The emission point is $\boldsymbol{x}_e = (0, 0, 2.5)$ and the reception point is in the far zone ($|\boldsymbol{x}_r| \gg |\alpha|$) on the positive x-axis, outside the figure. The line of sight from $\boldsymbol{x}_e$ to $\boldsymbol{x}_r$ is indicated by the long arrow.

decays as a Gaussian in $r - r_r - r_e$ perturbed by $\tilde{H}_d(-\mathrm{i}(r - r_r - r_e))$. Combined with the effect of the derivatives coming from $\partial_{\alpha'\alpha}$, this perturbation displaces the maximum from the line of sight ($r_r + r_e = r$) to a small circle centered at the line-of-sight point. The derivatives cause $\mathcal{I}_d^\alpha$ to vanish at the line-of-sight point and oscillate near the circle, thus creating the ring pattern seen in figure 12.

For the two complex spheres in the middle and bottom plots, $\tilde{g}_d(t - \zeta)$ suppresses the points $R\hat{\boldsymbol{n}}$ with $\eta_r \leqslant \eta_e$ and boosts those with $\eta_r > \eta_e$ in the frontal zone S_R^+ of (47).

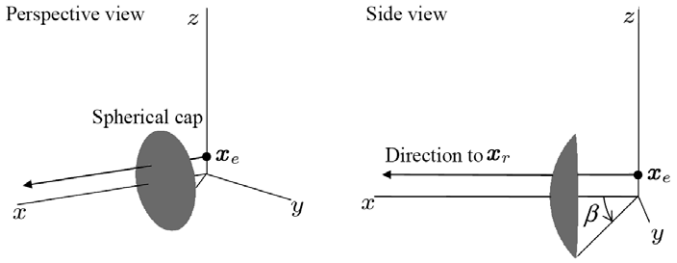

Figure 13. A spherical cap with cap angle β centered on the x-axis.

Simultaneously $g_d(r-\xi)$ suppresses points with $|r-\xi| > d$, and the winners of this tug of war are the points in the small spot centered at $R\hat{\boldsymbol{x}}_r$ in the middle and bottom plots of figure 12. This spot becomes more and more concentrated near $R\hat{\boldsymbol{x}}_r$ with increasing a.

It is important to note that $\mathcal{I}_d^\alpha$ for large a is concentrated around the point $R\hat{\boldsymbol{x}}_r$ nearest to the receiver *regardless of the location of the emission point.* This means that $\mathcal{I}_d^\alpha$ for large a would remain concentrated near $R\hat{\boldsymbol{x}}_r$, as in figure 12, even if we replaced the point source at $\boldsymbol{x}_r$ with an arbitrary volume source $\varrho(x_e)$ supported throughout the interior of S_R. This can be understood by noting that a disk source becomes more *directive* with increasing radius; hence, fewer disks are required to achieve a given accuracy.

To illustrate the advantages of using complex spheres with large value of a, we investigate the accuracy of the field at $\boldsymbol{x}_r$ obtained by including only the pulsed beams radiated from a spherical cap centered around $R\hat{\boldsymbol{x}}_r$ with maximum angle β, as in figure 13. For the parameter values under consideration, $\beta_0 = 15^\circ$ represents a cap where the line of sight from $\boldsymbol{x}_e$ to $\boldsymbol{x}_r$ just grazes the upper edge of the cap. We compute the maximum error over all time of the field at $\boldsymbol{x}_r$, relative to the maximum value $g_d(0)/r$. This calculation is designed to simulate the realistic situation where the time dependence of the source is unknown and the source may emit a series of pulses that are spread out over time. In particular, the computed error bounds also hold for time-harmonic fields. Figure 14 shows this maximum error as a function of $\beta \geqslant \beta_0$ for the three values of a. A dramatic error reduction is obtained by increasing a. For example, the errors $\varepsilon(a)$ for $\beta = 45^\circ$ are

$$\varepsilon(0) = 27.9\%, \qquad \varepsilon(5) = 8.3\%, \qquad \varepsilon(50) = 1.5\%,$$

a reduction of nearly 20:1 when using the pulsed-beam representation with $a = 50$ compared to the real Huygens representation! This has important practical implications in numerical calculations, where a certain error level must be often achieved. For example, assume that the error of the field at the reception point must be less than 2%. Then the required cap angles $\beta(a)$ are

$$\beta(0) = 152^\circ, \qquad \beta(5) = 89^\circ, \qquad \beta(50) = 38^\circ.$$

Hence, with $a = 50$, we need to include pulsed-beam wavelets over just 11% of the sphere, whereas $a = 0$ would require spherical wavelets over 94% of the sphere.

Remark 2. Consider the efficiency of the 'alternate' expression using (86), whose negative-frequency component was obtained by letting $\alpha \to \alpha^*$ and $\alpha' \to \alpha'^*$ in the conjugate pulsed-beam expansion (75) of $\tilde{P}_d(\boldsymbol{x}, t)^*$. This gives the expression

$$P_d(\boldsymbol{x}, t) = \frac{\alpha^2}{4\pi} \int \frac{\mathrm{d}\hat{\boldsymbol{n}}}{\zeta_r \zeta_e} \left[\frac{\zeta_e'}{\zeta_e} - \frac{\zeta_r'}{\zeta_r} + (\zeta_e' - \zeta_r')\partial_t \right] g_d(t - \zeta) \equiv \int \mathrm{d}\hat{\boldsymbol{n}} \mathcal{J}_d^\alpha(\hat{\boldsymbol{n}}, t), \tag{112}$$

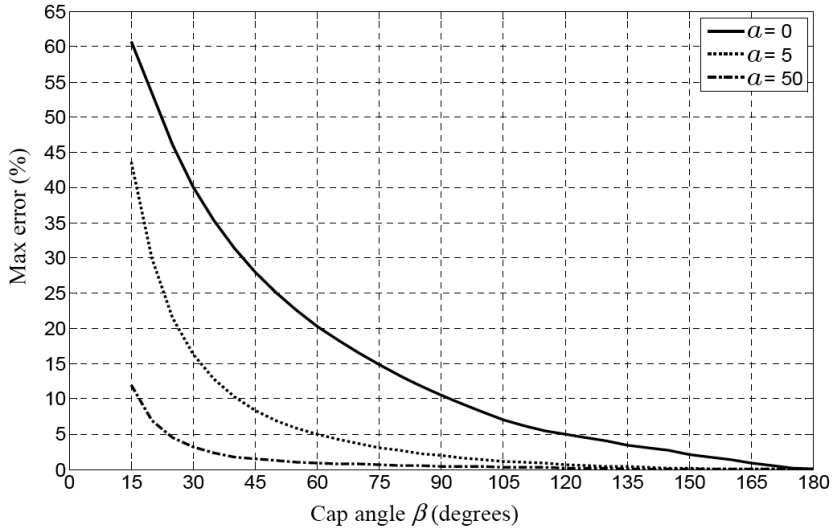

Figure 14. Compression: The maximum error at a far-zone reception point on the positive x-axis as a function of the cap angle β. The emission point is on the z-axis at $z = 2.5$. The three spheres have $R = 10$ with disk radii $a = 0$, $a = 5$ and $a = 50$.

where $\tilde{g}_d$ has been replaced by g_d in the integrand. As noted under (86), this means that the negative-frequency pulsed beams propagate along $-\hat{\boldsymbol{n}}$ instead of $\hat{\boldsymbol{n}}$, thus traversing the sphere and spoiling the efficiency of (74). To demonstrate the enormous difference between (111) and (112), consider again the complex sphere with $\alpha = 10 + 50\mathrm{i}$, $\boldsymbol{x}_e = (0, 0, 2.5)$ and $\boldsymbol{x}_r = (200, 0, 0)$ in the far zone. Since (112) does not have a factor like $\tilde{H}_d$, there will be significant contributions from the backside of the sphere. In particular, consider

$$\hat{\boldsymbol{n}} = -\hat{\boldsymbol{x}}_r = (-1, 0, 0) \;\Rightarrow\; \zeta = \zeta_r + \zeta_e = 220.01 + 99.94\mathrm{i}.$$

Choosing $d = 0.3\sqrt{2}$ as before and $t = \xi = 220.01$, we find

$$g_d(t - \zeta) = g_d(-99.94\mathrm{i}) = 1.33\,\mathrm{e}^{55\,489} \sim 10^{25\,000}.$$

The contribution from the back point $-\hat{\boldsymbol{x}}_r$ in (112) is seen astronomical! By comparison, the counterpart of $g_d(-99.94\mathrm{i})$ in (111) is

$$\tilde{g}_d(-99.94\mathrm{i}) = 0.001\,59.$$

This illustrates that (111) and (112) are on opposite sides of the computational efficiency spectrum.

Figure 14 suggests that the compression keeps increasing with a, and it is natural to wonder if there is an 'optimal' value of a beyond which the benefits of further increase will diminish. Asymptotic analysis in the far zone shows that as a increases, $\tilde{g}_d(t - \zeta)$ approaches zero everywhere on the sphere except at $\hat{\boldsymbol{n}} = \hat{\boldsymbol{x}}_r$, where its magnitude approaches $|\tilde{g}_d(t - r)|$. Moreover, $\tilde{g}_d(t - \zeta)$ decays smoothly without oscillations away from $\hat{\boldsymbol{n}} = \hat{\boldsymbol{x}}_r$. Hence, there is indeed no limit to how small the cap angle β can be for a given error limit. However, as a increases, the sampling rate used in the computation of the integral (111) must also be increased. We shall investigate the numerical consequences of using large values of a more fully in future work.

Acknowledgments

It is our pleasure to thank Dr Arje Nachman and the Air Force Office of Scientific Research for their support of this work. GK was supported by AFOSR grant #FA9550-08-1-0144. We also thank David Park for helping with the Mathematica graphics.

References

[AS70] Abramowitz M and Stegun I A 1970 *Handbook of Mathematical Functions* (Washington DC: National Bureau of Standards)

[BC87] Baker B B and Copson E T 1987 *The Mathematical Theory of Huygens' Principle* 3rd edn (New York: Chelsea)

[BW99] Born M and Wolf E 1999 *Principles of Optics* 7th edn (Cambridge: Cambridge University Press)

[CH89] Choi H C and Harris J G 1989 Scattering of an ultrasonic beam from a curved interface *Wave Motion* **11** 383–406

[C81] Couture M and Belanger P A 1981 From Gaussian beam to complex-source-point spherical wave *Phys. Rev.* A **24** 355–9

[D71] Deschamps G A 1971 Gaussian beam as a bundle of complex rays *Electron. Lett.* **7** 684–5

[D8] Devaney A J, Kaiser G, Marengo E A, Albanese R and Erdmann G 2008 The inverse source problem for wavelet fields *IEEE Trans. Antennas Propag.* **56** 3179–87 http://wavelets.com/pdf/8DKMAE.pdf

[F76] Felsen L B 1976 Complex-point-source solutions of the field equations and their relation to the propagation and scattering of Gaussian beams *Symp. Math. Inst. di alta Mat.* **18** 39–56

[F82] Felsen L B 1982 Geometrical theory of diffraction, evanescent waves and complex rays *Geophys. J. R. Astron. Soc.* **79** 77–88

[G64] Garabedian P R 1964 *Partial Differential Equations* (New York: Chelsea)
Garabedian P R 1998 *Partial Differential Equations* (Providence: AMS Chelsea)

[H6] Hansen T B 2006 Complex point sources in probe-corrected cylindrical near-field scanning *Wave Motion* **43** 700–12

[H89] Heyman E 1989 Complex source pulsed beam representation of transient radiation *Wave Motion* **11** 337–49

[H9] Hansen T B 2009 Complex point receiver formulation of spherical near-field scanning of acoustic fields using higher-order probes *Wave Motion* at press (doi:10.1016/j.wavemoti.2009.06.013)

[H9A] Hansen T B 2009 Complex-point dipole formulation of probe-corrected cylindrical and spherical near-field scanning of electromagnetic fields *IEEE Trans. Antennas Propag.* **57** 728–41

[HN97] Hansen T B and Norris A N 1997 Exact complex source representations of transient radiation *Wave Motion* **26** 101–15

[HY99] Hansen T B and Yaghjian A 1999 *Plane-Wave Theory of Time-Domain Fields: Near-Field Scanning Applications* (Piscataway, NJ: IEEE)

[K63] Kerr R P 1963 Gravitational field of a spinning mass as an example of algebraically special metrics *Phys. Rev. Lett.* **11** 237–8

[K90] Kaiser G 1990 *Quantum Physics, Relativity, and Complex Spacetime* (Amsterdam: North-Holland) available at http://wavelets.com/pdf/90NH.pdf

[K94] Kaiser G 1994 *A Friendly Guide to Wavelets* (Cambridge, MA: Birkhäuser Boston)

[K0] Kaiser G 2000 Complex-distance potential theory and hyperbolic equations *Clifford Analysis* ed J Ryan and W Sprössig (Cambridge, MA: Birkhäuser Boston) http://arxiv.org/abs/math-ph/9908031

[K3] Kaiser G 2003 Physical wavelets and their sources: real physics in complex spacetime *Top. Rev. J. Phys.* A **36** R29–R338 http://arxiv.org/abs/math-ph/0303027

[K4] Kaiser G 2004 Making electromagnetic wavelets *J. Phys. A: Math. Gen.* **37** 5929–47 http://arxiv.org/abs/math-ph/0402006

[K4a] Kaiser G 2004 Distributional sources for Newman's holomorphic Coulomb field *J. Phys. A: Math. Gen.* **37** 8735–45 http://arxiv.org/abs/gr-qc/0108041

[K5] Kaiser G 2005 Making electromagnetic wavelets: II. Spheroidal shell antennas *J. Phys. A: Math. Gen.* **38** 495–508 http://arxiv.org/abs/math-ph/0408055

[K67] Kellogg O D 1967 *Foundations of Potential Theory* (New York: Springer)

[KS71] Keller J B and Streifer W 1971 Complex rays with an application to gaussian beam *J. Opt. Soc. Am.* **61** 40–3

[NJ65] Newman E T and Janis A I 1965 Note on the Kerr spinning particle metric *J. Math. Phys.* **6** 915–7

[N65] Newman E T, Couch E C, Chinnapared K, Exton A, Prakash A and Torrence R 1965 Metric of a rotating, charged mass *J. Math. Phys.* **6** 918–9

[N73] Newman E T 1973 Maxwell's equations and complex Minkowski space *J. Math. Phys.* **14** 102–3

[N86] Norris A N 1986 Complex point-source representation of real point sources and the Gaussian beam summation method *J. Opt. Soc. Am.* A **3** 2005–10

[NH97] Norris A N and Hansen T B 1997 Exact complex source representations of time-harmonic radiation *Wave Motion* **25** 127–41

[S98] Stimson G W 1998 *Introduction to Airborne Radar* 2nd edn (Mendham, NJ: SciTech Publishing)

[TPB7] Tap K, Pathak P H and Burkholder R J 2007 Exact complex source point beam expansion of electromagnetic fields from arbitrary closed surfaces pp 4028–31 *2007 IEEE Antennas and Propagation International Symposium*

[TPB7A] Tap K, Pathak P H and Burkholder R J 2007 Fast complex source point expansion for accelerating the method of moments pp 986–9 *Int. Conf. on Electromagnetics in Advanced Applications 2007 (ICEAA 2007)*

[ZSB96] Zeroug S, Stanke F E and Burridge R 1996 A complex-transducer-point model for finite emitting and receiving ultrasonic transducers *Wave Motion* **24** 21–40